AD NUMBER

AD913411

NEW LIMITATION CHANGE

TO

Approved for public release, distribution unlimited

FROM

Distribution authorized to U.S. Gov't. agencies only; Test and Evaluation; May 1972. Other requests shall be referred to Naval Ship Research and Development Center, Bethesda, MD.

AUTHORITY

USNSRDC ltr, 24 Apr 1974

TWO-DIMENSIONAL SUBSONIC WIND TUNNEL INVESTIGATIONS OF A CAMBERED 30-PERCENT THICK CIRCULATION CONTROL AIRFOIL

by

Robert J. Englar

Technical Note AL-201

May 1972

TWO-DIMENSIONAL SUBSONIC WIND TUNNEL INVESTIGATIONS OF A CAMBERED 30-PERCENT THICK CIRCULATION CONTROL AIRFOIL

by

Robert J. Englar

May 1972

Technical Note AL-201

TABLE OF CONTENTS

LIST OF FIGURES

SYMBOLS

A	Model slot area, ft^2
c	Chord length, ft
C_a	Axial force coefficient
C_d	Sectional profile drag coefficient measured from momentum loss in wake and corrected for additional mass efflux of the jet
$C_{d_{rake}}$	Section profile drag coefficient as measured by rake, uncorrected
C_{d_e}	Equivalent drag coefficient, Equation (8)
C_ℓ	Sectional lift coefficient
$C_{\ell_{max}}$	Maximum sectional lift coefficient obtainable within test C_μ limitations
$C_{m_{c/4}}$	Pitching moment coefficient about the quarter-chord
$C_{m_{c/2}}$	Pitching moment coefficient about the half-chord
C_n	Normal force coefficient
C_p	Pressure coefficient, $\frac{p_\ell - p_\infty}{q_\infty}$
C_μ	Momentum coefficient, $\dot{m}V_j/(q_\infty S)$
d_{meas}	Measured profile drag corrected for jet mass efflux, lbs
d_e	Equivalent drag, lbs, Equation (7), (10)
h	Slot height, ft (except where noted)
h_t	Tunnel test section height, ft
ℓ	Sectional lift, lb
ℓ/d_e	Equivalent section lift-drag ratio

$\dot{m}$	Mass efflux, slugs/sec
P_{comp}	Compressor power required to generate airfoil corresponding C_μ
P_ℓ	Local static pressure on the model, lb/ft^2
P_{t_d}	Duct (plenum) total pressure, lb/ft^2
P_{t_∞}	Freestream total pressure, lb/ft^2
P_{t_r}	Total pressure measured by wake rake probes, lb/ft^2
P_∞	Freestream static pressure, lb/ft^2
q_∞, q	Freestream dynamic pressure, lb/ft^2
r	Trailing edge radius, ft
R	Universal gas constant
R_e	Reynolds number based on chord
S	Model planform area, ft^2
T_t	Jet total temperature, $^\circ R$
t	Airfoil maximum thickness, ft
V_j	Jet velocity, ft/sec $\left\{\frac{2\gamma}{\gamma-1} RT_t \left[1- \left(\frac{P_\infty}{P_{t_d}}\right)^{\frac{\gamma-1}{\gamma}}\right]\right\}^{\frac{1}{2}}$
V_∞, V	Freestream velocity, ft/sec
x	Chordwise distance from leading edge, ft
x_s	Slot position from leading edge, ft
x/c	Dimensionless chordwise position
y_s	Slot vertical position, ft
α_{geo}	Geometric angle of attack, deg
α_{eff}	Effective angle of attack, deg

α_c	Blade collective angle, deg
α_s	Rotor shaft angle, deg
η	Dimensionless spanwise position on rotor blade, distance from center of hub
μ	Rotor advance ratio, V_∞/V_{tip}
δ	Vertical displacement of cambered mean line

SUMMARY

A relatively thick Circulation Control (CC) elliptic airfoil section with thickness-to-chord ratio of 0.30 and a circular arc camber of 1.5 percent at the midchord was tested subsonically to determine its aerodynamic properties as a midspan blade section on a blown helicopter rotor. The two-dimensional tests established the section's ability to generate the required lift at low and negative incidence. Lift coefficients up to 6.5 were produced at moderate momentum coefficient ($C_\mu \leq 0.24$). High drag of the unblown bluff ellipse was greatly reduced by the application of very moderate blowing, and equivalent efficiencies of 47 (including power required for blowing) were generated at $C_\ell \approx 1.9$. The section's performance was found to be heavily influenced by upper and lower aft surface flow separations, especially at the larger positive and negative angles of attack. In addition, both low Reynolds number and an increase in slot height were detrimental to section lift capability. Nevertheless, the ability to operate at high lift coefficients essentially independent of angle of attack, and with large lift augmentation for relatively low blowing, promises to provide an effective blade section for heavy lift application.

INTRODUCTION

Recent wind tunnel investigations on circulation control (CC) airfoils employing tangential blowing over bluff trailing edges have demonstrated the very high lift potential of these profiles (References 1 through 6). Due to the phenomenon known as the Coanda effect, the jet sheet remains attached to the rounded trailing edge as a result of a balance between centrifugal force and the suction produced on the surface by the jet velocity. Entrainment of the upper aft surface flow initially yields a boundary layer control, but the principal effect is produced by the movement of the aft stagnation point to the underside of the airfoil. Coupled with a corresponding movement of the leading edge stagnation point, this yields a large increase in effective camber and circulation around the airfoil, and thus very high lift augmentation at relatively low mass flow rates. The high lift augmentations available at negative local inflow angles characteristic of rotor blades immediately suggest application to rotary wing vehicles. In addition, lift obtained by mass flow variation rather than be incidence change can eliminate mechanical cyclic blade pitch and associated vibrations. Based on these expected benefits, a four-bladed model circulation control rotor design and test were undertaken at NSRDC. Blade design was based upon a thick elliptic CC section at the root (subsonic characteristics taken from Reference 2) and a cambered thin CC ellipse at the tip (low speed data from Reference 3 and transonic data from Reference 7). It was the purpose of the present tests to evaluate the characteristics of a midspan blade section to effectively join these extremes of the CC rotor blade.

DESIGN CONSIDERATIONS

Preliminary rotor flow field analyses were performed on the proposed CC rotor operating at various advance ratios, shaft and collective angles, thrust coefficients, and spanwise blade loadings. Figure 1 shows sample ranges of lift coefficient and effective incidence (α_{eff}), where the closed dotted curves represent a 360° cyclic variation (one per rev)

around the rotor azimuth at constant collective and shaft angles. The solid curve represents the limiting boundary of C_ℓ vs α_{eff} based upon a large sample of the dotted curves. It covers the range of lifting requirements which must be met by the blade section near midspan. Thus, the section must be capable of $C_\ell \approx 6$ at $-5^\circ \leq \alpha_{eff} \leq 2^\circ$, while still yielding high C_ℓ for $\alpha_{eff} = -10^\circ$ or less. For simplicity, the constraints of linear variation in thickness, and no blade twist or taper were imposed on the rotor design. This led to a thickness-to-chord ratio of 0.30 for the present model at a spanwise position of $\eta = 0.62$, approximately midway between the 50% thick ellipse at $\eta = 0.10$ and the 15% thick ellipse at the tip ($\eta = 1.0$). Although extensive data for the 50- and 15-percent thick ellipses were already available (References 2, 3, and 7), the characteristics of these two sections were so different that an attempt to extrapolate between them for the midspan section data could be very misleading. It was thus decided to construct and test the linearly prescribed 30-percent thick ellipse for the 62-percent span station.

The geometric characteristics of this 30% ellipse were determined from potential flow pressure distributions at the required C_ℓ and α_{eff} for a variety of camber and trailing edge radius values. Blowing slot location and height were determined based on past test experience, and inviscid pressure distributions. (A more detailed discussion of the design procedure for circulation control airfoils is given in References 8 and 9). As stated in Reference 8, it is desirable from the standpoint of maintaining strongly attached Coanda flow to provide a slot height-to-radius ratio of $h/r \leq 0.05$. In order to produce effective Coanda turning and reduce high suction peaks, a trailing edge radius-to-chord ratio of $0.02 \leq r/c \leq 0.05$ is advisable. These two parameters yield approximately $0.0005 \leq h/c \leq 0.0025$. Figure 2 depicts the effects of trailing edge radius increase, showing the associated increase in and forward movement of the trailing edge suction peak. The position of this aft suction peak is important from the standpoint of the adverse pressure gradient immediately downstream of it. To be effective, the slot should be located just upstream of the adverse gradient, so as to prevent the separation tendencies produced by the sudden pressure rise. Although a more forward slot location delays section stall (due to boundary layer control), it also reduces lift augmentation

since the jet sheet will have a reduced momentum by the time it reaches the trailing edge. Aft suction peaks allow aft slot location, momentum excess in the jet at the trailing edge, and high lift augmentations. To produce these conditions, the pure elliptic trailing edge radius-to-chord ratio (r/c = 0.045) was increased to 0.06 based on plots similar to Figure 2. It was anticipated that this slight increase in r/c above the recommended limit of 0.05 would provide additional Coanda effectiveness to assure high lift augmentation. Figure 2 shows that this choice produces almost no change in the location of the adverse pressure gradient, and only a slight increase in the suction peak. As Figure 1 does not indicate the requirement for operation at large positive incidence, the aft slot location and preference for negative α were compatable. The choice of section camber is also closely related to the reduction in leading and trailing edge suction peaks, as an increase in camber will generally reduce these peaks (at constant C_ℓ), spreading the upper surface suction more heavily over the central portion of the section. (At very high lift, suction peaks can produce undesirable compressibility effects.) For the present airfoil, the amount of camber was determined by the characteristics of the proposed tip section. As this thin section was primarily designed for transonic operation (see Reference 7), its trailing edge geometry was not the optimum for high lift on the retreating side of the rotor azimuth. This was compensated for by incorporation of 2.5% circular arc camber (i.e., δ/c = .025) to provide additional low speed lift. The linear camber variation from blade tip to uncambered root thus required the mid span 30% ellipse section to have approximately 1.44 percent circular arc camber.

MODEL AND TEST APPARATUS

MODEL

Based on the design considerations of the previous section, the following geometric and dimensionless parameters were applied to an analytically defined ellipse of 30 percent thickness-to-chord (minor-to-major axis) ratio:

chord	$c = 5.99"$	
thickness	$t = 1.83"$	$t/c = 0.3053$
circular arc camber	$\delta_{max} = 0.09"$	$\delta_{max}/c = .0149$
trailing edge radius	$r = 0.36"$	$r/c = 0.0601$
slot position	$x_s = 5.78"$	$x_s/c = 0.9640$
	$y_s = 0.36"$	$y_s/c = .0601$
slot height	$h = 0.02"$	$h/c = 0.00333$
	$0.01"$	0.00167
	$0.005"$	0.00083

The 5.99-inch model chord length was based upon two considerations: (1) keep relative thickness of the model small to prevent large tunnel blockage, and (2) restrain chord length such that chord-to-tunnel height ratio (c/h_t) would be less than 0.30 so that wall constraint (streamline curvature) corrections would be small and could be accurately estimated by existing techniques (References 10, 11 and 12).

Details of the model are shown in Figure 3. The section is constructed of 0.25 inch fiberglass finished to 600 fineness, with the aft upper surface formed by a contoured steel blade which also served as the upper boundary of the slot. The exit of the slot was contoured to be the minimum area throat of a smoothly converging nozzle, whose height was adjustable by means of fine pitch screws. An undercut or bevel in the blade near the nozzle throat assured that the flow would exit from the slot as near tangent to the surface as possible. (Failure to meet this tangency condition can produce a local region of jet detachment followed by re-attachment immediately downstream of the slot - this can be energy-absorbing if the resulting bubble becomes large.) Additional construction details of similar models are found in References 1, 2, 3 and 7.

TEST APPARATUS AND TECHNIQUE

The two-dimensional tests were conducted in the NSRDC 15 x 20-inch subsonic tunnel with vented test section and plexiglass walls for flow visualization. Test technique employed was identical to that used with the two 15-percent thick ellipses of Reference 3; and will thus only be mentioned briefly. The model was pressure tapped at the centerspan for determination of lift and pitching moment coefficients, while a total head

wake rake was used for drag. As very high lift and severe adverse pressure gradients were generated, strong three-dimensionality and induced effects were present in the uncorrected test conditions. These could virtually invalidate all high lift results, and thus the addition of internal blowing plenums (tip jets) at the model-wall junction was necessary to energize the wall boundary layer and prevent its separation and the resulting vorticity. These plenums and their use are thoroughly described in References 3 and 6, while a detailed discussion of the many problems associated with high-lift 2-D testing and their solutions comprises the main text of Reference 13. As some wall separations at the model nose were not completely controlled by the plenums, relatively large flow fences were installed on the model within 0.5 inches of the wall to prevent interference at the midspan measuring station. Spanwise pressure taps and cotton tufts were used to indicate the two-dimensionality of the flow.

Mass flow rate ($\dot{m}$) was measured using an orifice plate which had been calibrated for Reynolds number based on opening diameter, while jet velocity (V_j) was calculated assuming an isentropic expansion from measured internal duct pressure to freestream static pressure. The non-dimensional product of these two terms yielded the momentum coefficient

$$C_\mu = \frac{\dot{m}V_j}{qS} \qquad (1)$$

DATA CORRECTIONS

Conventional corrections (for example, References 10 and 12) were applied to measured freestream dynamic pressure to account for solid blockage due to model thickness, but no wake blockage corrections were applied due to the varying effect of the tangential jet on wake size. Care was given to measuring the freestream q in the test section, as large disturbances propagated upstream at high lift and altered the q as measured by the calibrated piezometer ring at the test section entrance. It was found that the least affected value was obtained using the static pressure tap located midway up the sidewall as far upstream in the test section as possible. The validity of the freestream dynamic pressure yielded by use of this tap and corrected for solid blockage was proven by the generation

of $C_p = 1.0$ at the leading edge stagnation point, which is easily located due to the smoothly distributed pressure over the bluff nose. Dynamic pressure used to nondimensionalize drag was determined from static pressure at the rake station, which was slightly different from the upstream value due to the bouyancy effect (See Reference 13).

After using the corrected value of q to determine the lift and moment coefficients, these could be further corrected for tunnel wall constraint (induced camber, i.e., lift interference) as follows, where subscript u denotes the uncorrected value:

$$\alpha = \alpha_u + \frac{57.3\pi c^2}{96 h_t^2} \left(C_{\ell_u} + 4C_{m_{25_u}}\right) = \alpha_u + 0.1687\left(C_{\ell_u} + 4C_{m_{25_u}}\right) \qquad (2)$$

$$C_\ell = C_{\ell_u}\left(1 - \frac{\pi^2}{48}\frac{c^2}{h_t^2}\right) = 0.9815\, C_{\ell_u} \qquad (3)$$

$$C_{m_{25}} = C_{m_{25_u}} + \left(\frac{\pi^2}{48}\frac{c^2}{h_t^2}\right)\frac{C_\ell}{4} = C_{m_{25_u}} + .00463\, C_\ell \qquad (4)$$

$$C_{m_{50}} = C_{m_{25}} + \frac{C_\ell}{4} = C_{m_{25_u}} + .00463\, C_\ell + \frac{C_\ell}{4} \qquad (5)$$

As these corrections are valid to the second power of chord/tunnel height only when $c/h_t \leq 0.30$ and were derived for thin unflapped airfoils, the present model ($c/h_t = 0.30$) is a border line case, and thus the data presented have not been corrected using them. The error introduced by using the uncorrected values is estimated to be small (3 percent or less). Furthermore, comparison of experimental data with results in unconstrained

potential flow show negligible difference in the upper surface pressure at the midchord, where induced camber influence should be noticeable if present.

RESULTS AND DISCUSSION

Tests were conducted for three model slot heights over a geometric incidence range of $-30° \leq \alpha_{geo} \leq +8°$, a momentum coefficient range of $0 \leq C_\mu \leq .24$, and for dynamic pressures of 10, 20 and 40 psf. Test values of momentum coefficients and jet velocities are presented in Figure 4 and 5 as functions of slot height, duct total pressure, and freestream dynamic pressure. Upper limitations on C_μ were determined from pressure (structural) limits in the model, impingement of the jet on the tunnel floor, or trailing edge suction exceeding the operating range of the pressure transducers. Test dynamic pressure and Reynolds number were selected based on the results of Figure 6, in which test data for the unblown ellipse is plotted over a range of Reynolds numbers from 200,000 to 700,000. Leveling out of the lift and drag curves above R_e = 550,000 was observed and a dynamic pressure of 40 lb/ft^2 ($R_e \approx$ 570,000) was thus chosen as the test value above which lift and drag no longer varied significantly with Reynolds number for $C_\mu = 0$. This q value and the 3 limitations listed above placed an upper limit on C_μ of about 0.12. A second test q of 20 lb/ft^2 was thus chosen in order to extend the range of available C_μ to about 0.24. A very limited number of points were run at q = 10 lb/ft^2 to obtain the effects of very low Reynolds number.

LIFT

The sectional lift coefficients as determined from integration of midspan pressure distributions ($C_\ell = C_n \cos \alpha_{geo} - C_a \sin \alpha_{geo}$) are presented as functions of blowing coefficient at constant incidence, slot height and dynamic pressure in Figures 7, 8 and 9. For the relatively low limiting value of momentum coefficient ($C_\mu \approx .24$), lift coefficients as high as 6.5 were obtained for this mono-element airfoil. The initial sharp rise in the C_ℓ vs C_μ curve at low blowing is usually attributed to boundary layer control, while the gradual reduction in curve slope at somewhat

higher C_μ indicates a transition to the phenomenon of supercirculation. Even at the large negative incidence of -30°, the increased circulation is still able to produce positive lift. Figure 10 shows that, of the three slot heights tested, the smallest value (h = .005 inch) yielded the best lifting performance at the same C_μ; degradation in lift coefficient with increased slot height is evident in this figure. For a constant C_μ, an increase in slot height implies a decrease in jet velocity over the trailing edge (see Figure 5), and thus a decrease in jet kinetic energy (proportional to V_j^3). This reduced energy flux apparently reduced the turning ability of the Coanda jet. Likewise, mixing of the larger jet with the upper surface boundary layer may result in energy losses and adversely affect performance. The implication is that the smallest possible jet height should be most effective, yet there are limitations here also. A smaller slot height implies increased jet velocities which could cause choking in the throat and expansion to supersonic flow; the eventual pressure rise from recompression of this supersonic flow may produce jet detachment. In addition, boundary layer buildup in very small nozzles can cause loss of performance (see Reference 3). Considering these tradeoffs for the h = 0.005 inch configuration, the majority of the test data were recorded for h = 0.01 inch, and thus this data comprises the remainder of the report. In addition, as Figure 10 shows, the 0.01-inch height does exhibit the greatest maximum efficiency (ℓ/d_e, to be discussed later) even though its net lift is less.

The curves of Figure 7 represent two values of dynamic pressure and Reynolds number. The majority of the data (plain symbols) was run at $q = 40$ lb/ft², $R_e \cong 570{,}000$ and $V = 195$ ft/sec. However, as previously mentioned, an upper C_μ limit of 0.12 was associated with this condition due to jet impingement on the tunnel floor and pressure differentials exceeding transducer limits. Thus, additional points were run at half the dynamic pressure ($q = 20$ lb/ft², $V = 137$ ft/sec, $R_e \cong 407{,}000$), which doubled the limit on C_μ to 0.24 for the same duct pressure. As can be seen from the points in the lower C_μ range of Figure 7, a Reynolds number effect is present between dynamic pressures of 20 and 40 lb/ft²-this is shown more clearly in Figure 11, where the lift degradation at very low Reynolds

number is seen (This figure is a crossplot of Figure 7 and the low q data of Figure 12 (q = 10 lb/ft^2, R_e = 298,000, V = 96 ft/sec). Rather than incorrectly extrapolating for Reynolds effects in Figure 7, smooth curves were drawn through the data for q = 20 and 40 psf - they are thus somewhat conservative at $C_\mu > 0.12$, since the actual C_ℓ should be greater than shown.

Figure 13 depicts the high lift augmentations delivered by the 0.01-inch slot configuration, where the parameter $\frac{\Delta C_\ell}{\Delta C_\mu}$ is defined as the increase in lift coefficient (above the unblown value) for a given amount of blowing at constant incidence. With the exception of the large negative incidences (-20° and -30°) and the 8° incidence, the data all fall within a relatively narrow band, indicating nearly parallel C_ℓ vs C_μ curves in Figure 7 - the curves are offset from each other at $C_\mu = 0$ by an amount of C_ℓ due solely to incidence. Within the range of C_μ tested, no lift drop-off (C_μ - stall) occurred with increasing blowing at constant incidence (except at q = 10 lb/ft^2 and high C_μ); it appears that considerably larger lift coefficients could have been generated with additional increases in blowing had test conditions allowed.

Further insight into the lifting capabilities of the thick blown airfoil is provided by the experimental pressure distributions of Figures 14 and 15. At zero incidence, supercirculation due to increased blowing produces the characteristic "saddle-back" pressure distribution. The trailing edge suction peak is produced by the higher velocities in the jet, while the nose peak is a result of increased flow acceleration around the leading edge due to the progressively aft movement of the lower surface stagnation point. Of interest is the lower aft surface pressure distribution, which is initially separated, but returns to attached flow with blowing, and then experiences a separation bubble at higher blowing. At large negative incidence (Figure 15), the lower surface flow remains completely separated at the lower blowing coefficients, but positive C_ℓ is still generated due to the jet. The leading edge stagnation point, which is on the upper surface, moves forward as the circulation increases due to blowing, and the lower surface finally reattaches. Again, a lower surface separation bubble is evident at the higher blowing rates. In both Figures 14 and 15, a small local separation on the upper surface is seen in the jet immediately downstream of the slot, but apparently little net effect is produced.

An interesting feature of tangential blowing over bluff trailing edges of elliptic sections is the apparent ability to generate conditions closely resembling inviscid flow. Figure 16 shows comparison between experiment and theory for geometric incidence of 4 degrees. With no blowing, disagreement occurs aft of mid-chord due to flow separation from the thick airfoil. However, for C_μ = .1886 the jet has entrained sufficient flow to cause reattachment. Agreement with the potential flow is quite good, with two exceptions: the increased velocity (and thus C_p) at the trailing edge due to the jet, and the lower surface trailing edge separation caused by the interaction of the jet and boundary layer. Neither of these conditions are predictable by a simple inviscid method. The incremental lift due to additional upper surface suction caused by the jet ($\Delta C_{\ell_{jet}}$) can be approximated empirically, and for unseparated flow appears to be independent of incidence as seen in Figure 17. The lower surface separation is usually negligible in lift obtained by pressure integration, and thus the potential flow prediction corrected for $\Delta C_{\ell_{jet}}$ can be a very close approximation to the lifting capabilities of circulation control airfoils.

Two additional items are necessary to complete the discussion of the 30 percent ellipse lifting characteristics: the induced effects in the experimental data caused by some spanwise non-uniformity; and a large deficit in the lift curve for 8° incidence in Figure 7. Relative to the induced effects, it was found that, even though tip jet and flow fences were both employed to assure two-dimensionality across the model, the very high lift coefficients still caused tunnel wall boundary layer separation and the resulting induced downwash (see Reference 13). As a result, the model was not operating at the geometric incidence, but at an effective incidence (α_{eff}) less than geometric. To determine what these effective angles were, potential flow pressure distributions (adjusted for $\Delta C_{\ell_{jet}}$) were generated for several incidences bracketing the geometric incidence at the corresponding C_ℓ. These curves were then compared to the experimental pressure distributions until the lower surface leading edge stagnation points coincided, which identified the correct effective incidence for each C_ℓ. These results are plotted in Figure 18 for lines of constant geometric incidence. Plotted also for comparison is data for the 20 percent thick CC ellipse of Reference 5, which had only small flow fences and no tip jets to maintain

two-dimensionality. The difference between the $\alpha_{geo} = 0^{\circ}$ slopes for the two tests indicates the improved effectiveness of the tip jet-large flow fence combination of the present tests in controlling the induced effects. It should be noted that these induced angles ($\alpha_{geo} - \alpha_{eff}$) may still be as much as 5 degrees at the high C_{ℓ} values. Figure 19 is a corrected plot of Figure 7, showing C_{ℓ} generated at constant effective incidence; the result for constant C_{μ}, is the generation of the same C_{ℓ} at a reduced true incidence. Figure 20 is a more conventional display of lifting ability, showing C_{ℓ} as a function of both α_{geo} and α_{eff} for constant values of momentum coefficient. The high lift available at large negative incidence is quite evident, while it is appraent that the lift requirement originally specified in Figure 1 can be obtained by the section.

In Figure 7, the large deviation at $\alpha_{geo} = 8^{\circ}$ (and $\alpha_{geo} = 4^{\circ}$ to a lesser extent) from the family of curves is apparently due to upper surface aft separation at positive incidence with low to moderate blowing (at $C_{\mu} > .14$, the curve returns to the same shape as the rest of the family of curves). The same phenomenon was observed in References 2 and 5, with the onset apparently occurring at lower incidence for thicker ellipses. Data from Reference 2 indicates that the return to the expected curve approaches a step function in C_{μ}, while Reference 5 mentions a hysteresis effect with tufts showing intermittent separation and reattachment that was not repeatable. The experimental pressure distribution of Figure 21 closely matches the potential flow (corrected for $\Delta C_{\ell_{jet}}$) even over the aft upper surface ahead of the slot, and flow separation is only slightly apparent. Also shown in this Figure is the pressure distribution for the "expected" lift coefficient (dotted line in Figure 7). It is seen that the gradual increase in suction (due to flow entrainment) towards the slot location for the "expected" distribution (see also Figure 14 high lift cases) is not present in the experimental distribution. This lack of flow extrainment evidently has a large effect on jet effectiveness; the maximum trailing edge suctic. peak of -4.8 (compared to -8.5 for the same $C_{\mu} = .101$ in Figure 14) indicates reduced Coanda effect and thus less supercirculation and lift. However, Figure 22 shows that with an increase in blowing to $C_{\mu} = .142$ at $\alpha_{geo} = 8^{\circ}$ the flow entrainment is re-established, the suction peak rises to $C_p = -10.7$ and the expected lift is almost completely restored.

The entire phenomenon could obviously prove quite detrimental to higher incidence operation of these thicker sections, especially in an unsteady rotating environment. More investigation need be undertaken to understand the flow mechanism involved if higher positive lift operation is ever anticipated for rotor blades.

DRAG

Drag measurements were made with a wake rake employing 54 total head probes and 8 static probes on a 15-inch high support located approximately 2 chords downstream of the model trailing edge. The momentum deficit methods of both Betz and Jones (Reference 14) were modified to account for the additional momentum of the jet as noted in References 1, 5 and 13. The modified drag coefficient then becomes

$$C_d = C_{d_{rake}} - \frac{\dot{m}V_\infty}{qS} = C_{d_{rake}} - C_\mu \frac{V_\infty}{V_j} \qquad (6)$$

This corrected drag coefficient is plotted in Figure 23 as a function of blowing coefficient and geometric incidence. As expected, the drag levels associated with the unblown cases are high due to the large momentum losses behind this thick bluff airfoil. However, as blowing is increased, flow entrainment into the jet reduces flow separation and thus overall drag, finally resulting in negative drag (a product of effective thrust recovery) for most of the incidences tested. Figure 24 presents sample total pressure measurements for the $\alpha_{geo} = -20°$ case, where the effect of blowing on reduction of the total head deficit is quite clear. An interesting "double" deficit appears for C_μ 0.0925, which corresponds to the sudden spike in the drag curves for negative airfoil incidence in Figure 23. Study of the model static pressure distribution reveals a distinct separation bubble which disappears with a slight increase in blowing. A similar double hump appears in Figure 25 for the $\alpha_{geo} = 8°$ data in the vicinity of $C_\mu = .10$, which corresponds to maximum drag for that incidence (Figure 23). The upper hump suggests (from its position relative to the previous cases for lower C_μ and from its nearness to the airfoil vertical location) that it is the conventional momentum deficit experienced behind a bluff body, accentuated in this instance by the large

amount of upper surface separation occurring on the section. The lower deficit seems to be indicative of a return to more effective operation (i.e., greater jet deflection), which has been nearly attained by the C_μ = .1418 case. In this latter data, the deficit is much lower in the vertical plane relative to the airfoil, and is probably a more direct result of mixing losses, as the Coanda turning is now greatly improved (see the lift data of Figure 7). The same trend may be true of Figure 24 as well, although upper surface separation preceeding this transition is not readily apparent. In practically all the data presented in Figure 23, it is clear that mixing losses (between jet and freestream), and separation (either upper surface, or a lower surface trailing edge region just ahead of the jet detachment point) play an important role. A detailed discussion of these considerations can be found in Reference 5.

Drag coefficient as a function of geometric incidence is presented in Figure 26, where it is seen that the low drag region extends further into the negative incidences than into the positive before a large increase in drag occurs. This results from a larger favorable pressure gradient ahead of the jet, and thus avoidance of the upper surface separation problems that arise for positive incidence.

PITCHING MOMENT

As has typically been the case with effective CC sections displaying strong Coanda attachment and turning, the suction peak generated by the jet at the trailing edge tends to produce negative pitching moments. These are reduced in magnitude by resolution about the section midchord instead of quarter-chord, as the midchord is likely to be the spar location on these thick helicopter blade sections. The slight camber of the airfoil tends to redistribute the chordwise loading more towards the midchord, thus reducing the nose suction peak which otherwise would have counteracted the jet suction peak and reduced the negative moments somewhat. Figure 27 presents the half-chord pitching moment as a function of blowing rate for the 0.01-inch slot height. Practically all values are negative with the exception of the separated flow values at $\alpha_{geo} = 8^p$.

EQUIVALENT LIFT-DRAG RATIO

Blown airfoil performance is best presented in terms of an equivalent lift-drag ratio, ℓ/d_e, where the equivalent drag term in the denominator

takes into account the measured drag as well as associated energy expenditures required to produce the blowing. This allows direct comparison with the efficiencies of unblown airfoils, and also avoids the unrealistic generation of infinite efficiencies when the measured drag of a blown airfoil becomes zero. In previous NSRDC reports (References 1, 2, 3, 6, 7, 8, 9 and 13), the equivalent drag has been derived from kinetic energy considerations of compressor power expended, and included an intake momentum flux:

$$\begin{aligned} d_e &= d_{meas} + \frac{\Delta KE}{V_\infty \, \Delta time} + \dot{m}V_\infty \\ &= d_{meas} + \frac{\dot{m}V_j^2}{2V_\infty} + \dot{m}V_\infty \end{aligned} \tag{7}$$

or in coefficient form, nondimensionalized by qS:

$$C_{d_e} = C_d + C_\mu \frac{V_j}{2V_\infty} + C_\mu \frac{V_\infty}{V_j} \tag{8}$$

The same equivalent drag may be obtained from momentum considerations and the control volume of Figure 28, where

$$\begin{aligned} d_e &= d_{friction} + d_{pressure} + d_{power\ input} + \Delta\ Momentum \\ &= d_{friction} + d_{pressure} + \frac{P_{comp}}{V_\infty} + \dot{m}V_\infty - \dot{m}V_j \end{aligned} \tag{9}$$

Drag as measured by a wake rake includes the first, second, and last terms of the second expression, but, as noted previously and in Reference 1, drag determined from the Jones or Betz momentum methods must be corrected to account for the added mass flux supplied to the test section. Then

$$d_e = d_{meas} + \frac{P_{comp}}{V_\infty} + \dot{m}V_\infty \tag{10}$$

The compressor power required to compress air from intake ram pressure to jet (plenum) total pressure is (from Appendix B of Reference 15):

$$P_{comp} = \frac{\dot{m}}{2}\left(\frac{2\gamma}{\gamma-1}\right)RT_t \left[1 - \left(\frac{P_{ram}}{P_{t_d}}\right)^{\frac{\gamma-1}{\gamma}}\right] \qquad (11)$$

If intake losses are assumed negligible, the ram pressure is identical to freestream total pressure, and thus, for $\gamma = 1.4$,

$$P_{ram} = P_{t_\infty} = P_\infty (1+ 0.2M_\infty^2)^{3.5}$$

For subsonic flows with $M_\infty \leq 0.2$, $P_{ram} \approx P_\infty$ and equation (11) becomes

$$P_{comp} = \tfrac{1}{2}\dot{m}V_j^2$$

which when substituted into (10) gives (7) and thus (8). The assumption of no intake losses reduces the power required since the pressure differential across the compressor is lower (P_{ram} is higher), while the small Mach number assumption does the reverse. As these two factors tend to be selfcancelling, it is concluded that equation (8) is sufficient to define an equivalent drag coefficient which is a fair basis for comparison to conventional airfoil efficiency.

An examination of the individual terms of the equivalent drag coefficient indicates that the measured drag is a relatively small or even negative contribution (see Figure 29). The key to obtaining high equivalent lift-drag ratios is appraently high lift augmentation (i.e., lift generation with minimum C_μ) which reduces the second and third terms for a given C_ℓ. The second term, a function of $(V_j/V_\infty)^3$, begins to dominate rapidly for all but the lowest values of C_μ. As can be seen in Figure 30, maximum efficiencies of approximately 47 occur at low incidence between 2 and 4 degrees and at $C_\ell \approx 1.9$. This value is roughly twice that of the lift coefficient corresponding to maximum ℓ/d for conventional rotor blade sections. Figure 31 presents blown ellipse maximum lift coefficient as a function of geometric and effective incidence and Figure 32 summarizes maximum efficiencies produced by variation in C_μ at a given incidence. Whereas there is a definite peak in the ℓ/d_e curve between 2 and 4 degrees geometric incidence, a limit in $C_{\ell max}$ has apparently not been reached

over the range of variables tested; increases in C_μ beyond 0.24 or α_{geo} above 8 degrees should yield greater values, even though corresponding efficiencies will be quite low.

Reference should again be made to Figure 10, where the peak value of $\ell/d_{e_{max}}$ from Figure 32 for h = 0.01 inch is plotted with corresponding values for h = 0.005 and 0.02 inch. It is seen that the 0.01 inch slot is 9 or 10 percent higher. The 0.005-inch configuration, even though it experiences somewhat greater lift, requires a greater jet velocity for the same C_μ, thus inflating the $(V_j/V_\infty)^3$ term in C_{d_e} and reducing $\ell/d_{e_{max}}$. The 0.02-inch slot suffers from reduced lift augmentation and also generates larger drag due to increased mixing losses of the thicker jet. Thus the majority of the data presented in this report corresponds to the most efficient of the slot heights examined, h = 0.01-inch.

CONCLUSIONS AND RECOMMENDATIONS

Subsonic two-dimensional tests conducted on the 30 percent thick circulation control ellipse indicated that this intended midspan section of the initial NSRDC CC rotor was able to obtain the lift requirements predicted over the entire range of blade operation. Experimental data obtained for variation of incidence, momentum coefficient, slot height, and Reynolds number yielded the following conclusions:

- The section was able to generate lift coefficients as high as 6.5 for $C_\mu \leq 0.24$, due primarily to the aft slot location and large trailing edge radius, which produced lift augmentations greater than 70. Relatively high C_ℓ values of from 2 to 4 were generated at large negative incidence of -20 to -30 degrees, but some lower surface separation was apparent.
- Initial (unblown) high drag levels on the bluff ellipse were easily reduced with relatively small amounts of blowing, but drag properties were heavily influenced by mixing losses and by upper and lower aft surface flow separations or bubbles.
- An apparent upper surface separation and loss of flow entrainment into the jet at higher positive angle of attack was responsible for very large lift losses and drag rise in the low to intermediate blowing range, $0 < C_\mu \approx .14$.

- Both low Reynolds number and an increase in slot height-to-chord ratio were found to have detrimental effects on section lift capability.
- Maximum section equivalent efficiencies (lift-drag ratios) of 47 were generated at low incidence and $C_\ell \approx 1.9$, roughly twice the C_ℓ corresponding to conventional unblown blade section maximum ℓ/d.

Recommendations for future work on thick, cambered CC sections would include:

- Investigation of upper surface flow phenomenon producing large lift degradation at positive incidence.
- Modification of aft lower surface to prevent boundary layer separation and separation bubbles, which apparently degrade both lift augmentation and drag.
- Testing at higher Reynolds number to identify the effects at higher blowing rates and on local flow separations.
- Testing of related thick configurations with increased camber and variation in slot location to improve section efficiency.

ACKNOWLEDGEMENT

The author would like to express his appreciation to Mr. M. Stone and Mr. J. Yablonsky for their assistance in both instrumentation and execution of the tests on the 30% ellipse, which were run in January through April, 1971.

REFERENCES

1. Williams, Robert M. and Harvey J. Howe. "Two Dimensional Subsonic Wind Tunnel Tests on a 20 Percent Thick, 5 Percent Cambered Circulation Control Airfoil." Wash., Aug 1970. (Naval Ship Research and Development Center. Tech Note AL-176) (AD 877-764)

2. Williams, Robert M. and Kenneth R. Reader. "Two-Dimensional Subsonic Wind Tunnel Tests on a 50-Percent Thick Circulation Control Airfoil with Blowing Slots Located at 88.6 and 98.5 Percent Chord." (Naval Ship Research and Development Center Tech Note AL-186) (In preparation)

3. Englar, Robert J. "Two-Dimensional Subsonic Wind Tunnel Tests of Two 15-Percent Thick Circulation Control Airfoils". Washington, Aug 1971. (Naval Ship Research and Development Center. Tech Note AL-211)

4. Jones, Dale G. "The Performance of Circulation Control Airfoils". Cambridge, Eng., Jul 1970. (Cambridge Univ. Ph.D. Thesis)

5. Kind, R. J. "A Proposed Method of Circulation Control". Cambridge, Eng., June 1967 (Cambridge Univ. Ph.D. Thesis)

6. Williams, Robert M. "Some Research on Rotor Circulation Control". In CAL/AVLABS Symposium: Aerodynamics of Rotary Wing and V/STOL Aircraft. 3rd Buffalo, Jun 1969. Proceedings, Vol. 2.

7. Englar, Robert J. "Two-Dimensional Transonic Wind Tunnel Tests of Three 15 Percent Thick Circulation Control Airfoils". Wash., Dec 1970. (Naval Ship Research and Development Center. Tech Note AL-182)

8. Englar, Robert J. and Robert M. Williams. "Design of a Circulation Control Stern Plane for Submarine Applications". Wash., March 1971. (Naval Ship Research and Development Center, Tech Note AL-200)

9. Williams, Robert M. "Design Considerations of Circulation Control Airfoils". (Naval Ship Research and Development Center. Tech Note AL-185), (In preparation)

10. Pope, Alan. "Wind-Tunnel Testing." 2nd ed. N.Y., John Wiley & Sons, Inc., 1964, p. 281-286

11. Van den Berg, B. "Some Notes on Two-Dimensional High-Lift Tests in Wind Tunnels." Presented at the AGARD-VKI lecture series on "Assessment of Lift Augmentation Devices", April 1970. (Netherlands National Aerospace Laboratory Paper, NLR MP 70008 U)

12. Garner, H. C., E. W. E. Rogers, et al. "Subsonic Wind Tunnel Wall Corrections." Paris, Oct 1966. (AGARDOGRAPH 109), p. 29-74.

13. Englar, Robert J. "Test Techniques for High-Lift Two-Dimensional Airfoils with Boundary Layer and Circulation Control for Application to Rotary Wing Aircraft". Paper presented at the Canadian Aeronautics and Space Institute Annual General Meeting "Practical Aspects of V/STOL Wind Tunnel Testing", May 1972.

14. Schlichting, Hermann. "Boundary Layer Theory". 6th ed., N.Y., McGraw-Hill, 1968.

15. Dods, Jules B. and Earl C. Watson. " The Effects of Blowing Over Various Trailing Edge Flaps on an NACA 0006 Airfoil Section, Comparisons with Various Types of flaps on Other Airfoil Sections, and an Analysis of Flow and Power Relationships for Blowing Systems". Washington, June 1956. (NACA Research Memorandum RM A56C01)

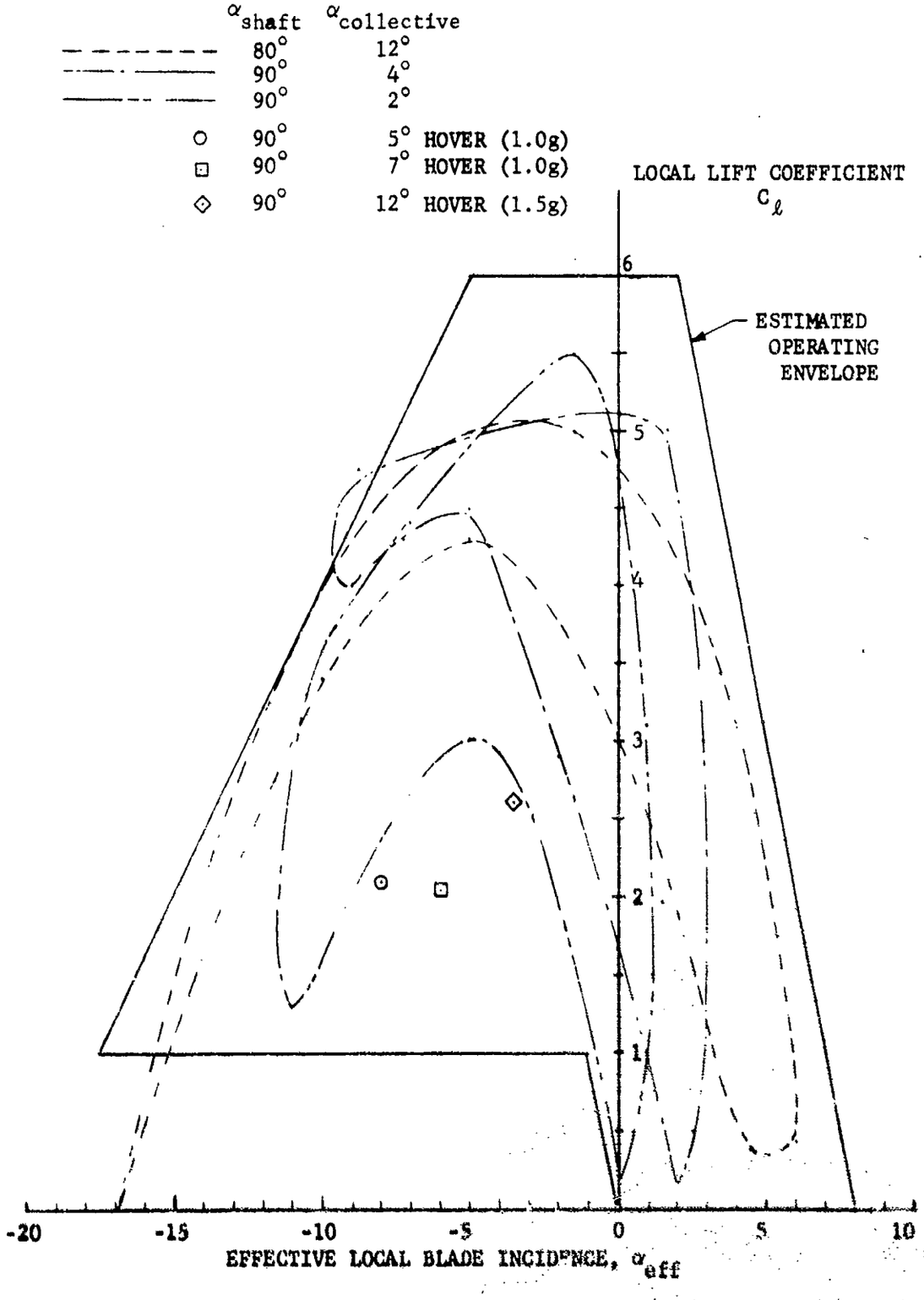

Figure 1 - Estimated Operating Range for Mid-Span Blade Section of Circulation Control Rotor (C_T = 0.0234, μ = 0.4, η = 0.55)

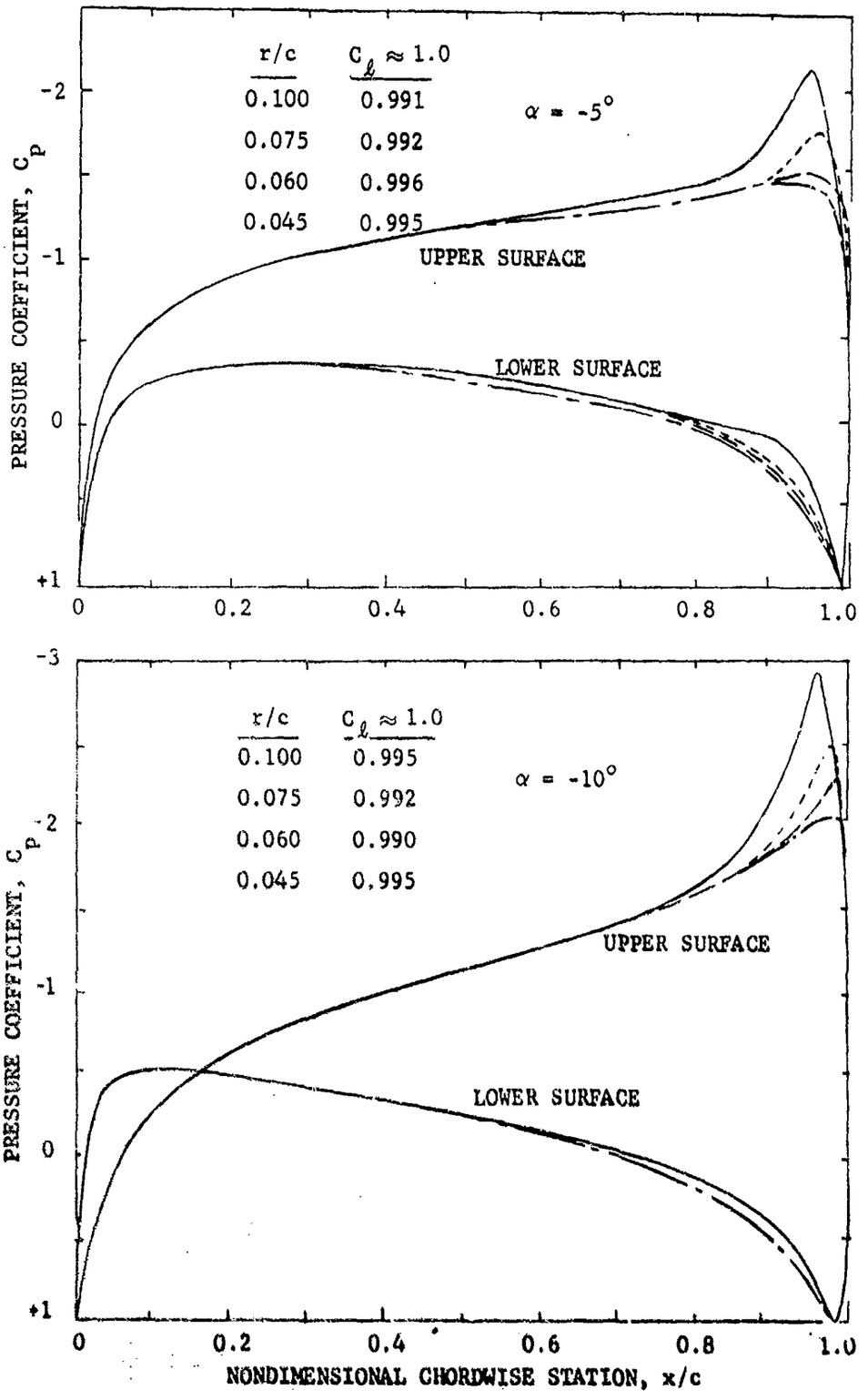

Figure 2 - Variation in Potential Flow Pressure Distributions with Change in Trailing Edge Radius on 30-Percent Ellipse with 1.25-Percent Camber

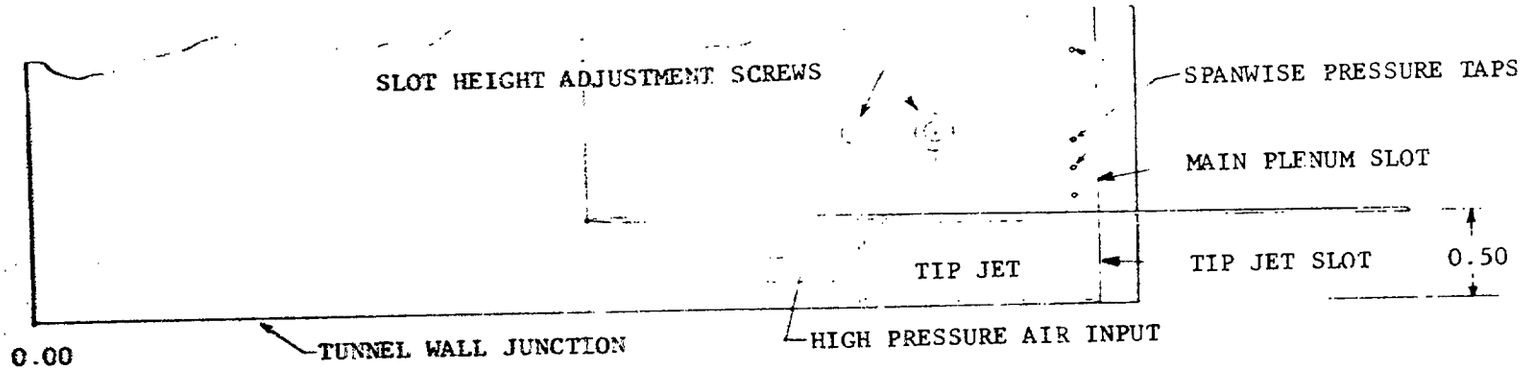

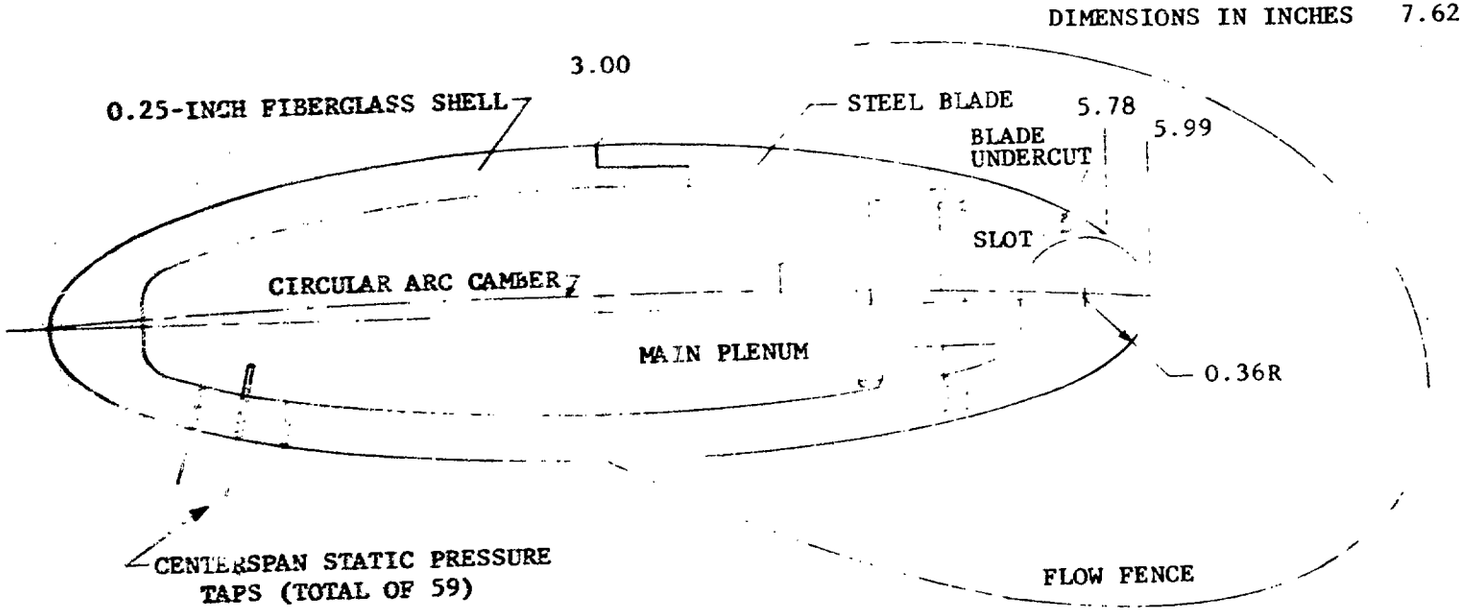

Figure 3 - Subsonic Two-Dimensional Model Geometry

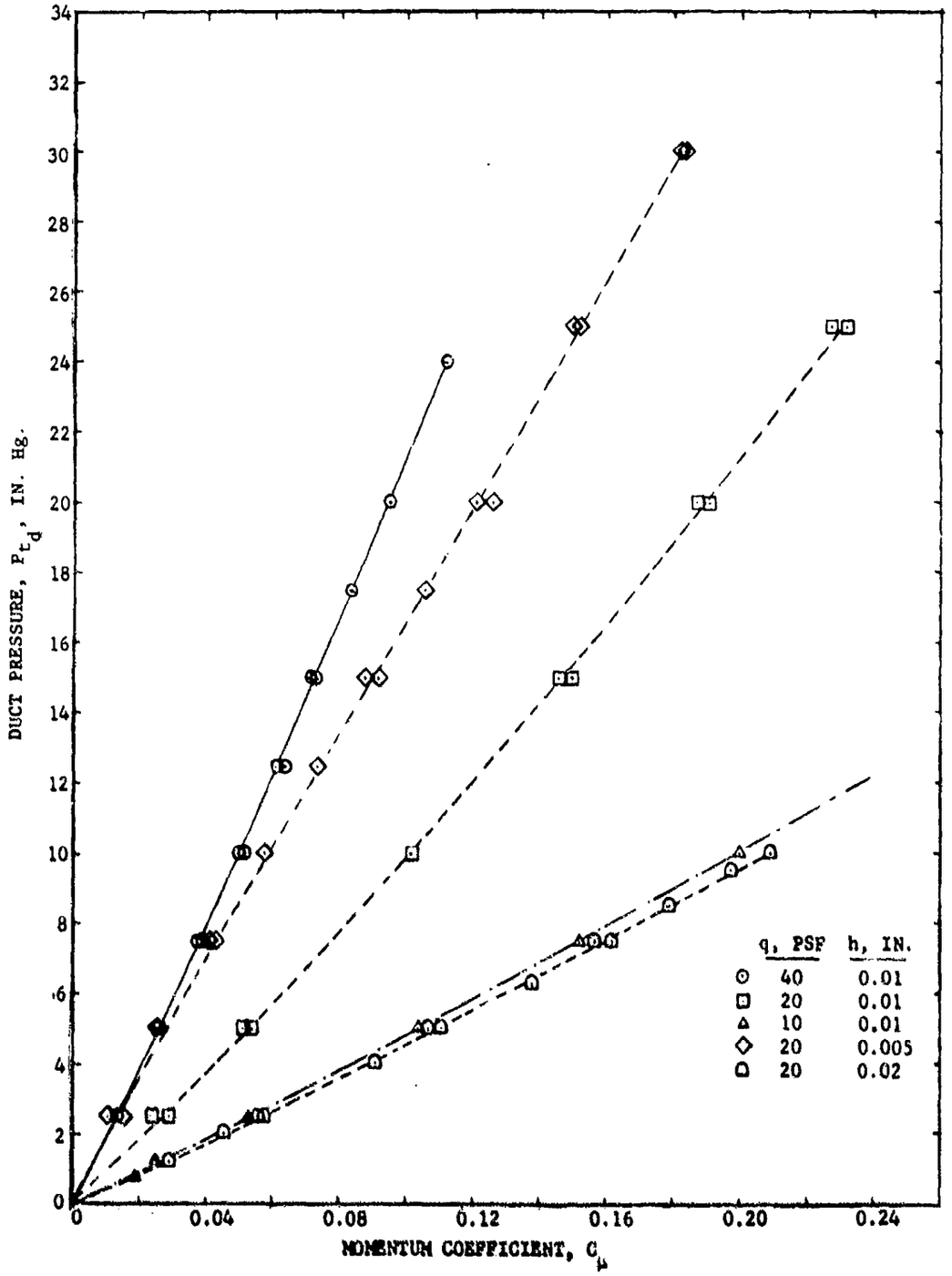

Figure 4 - Experimental Variation of Momentum Coefficient with Duct Pressure, Slot Height, and Dynamic Pressure

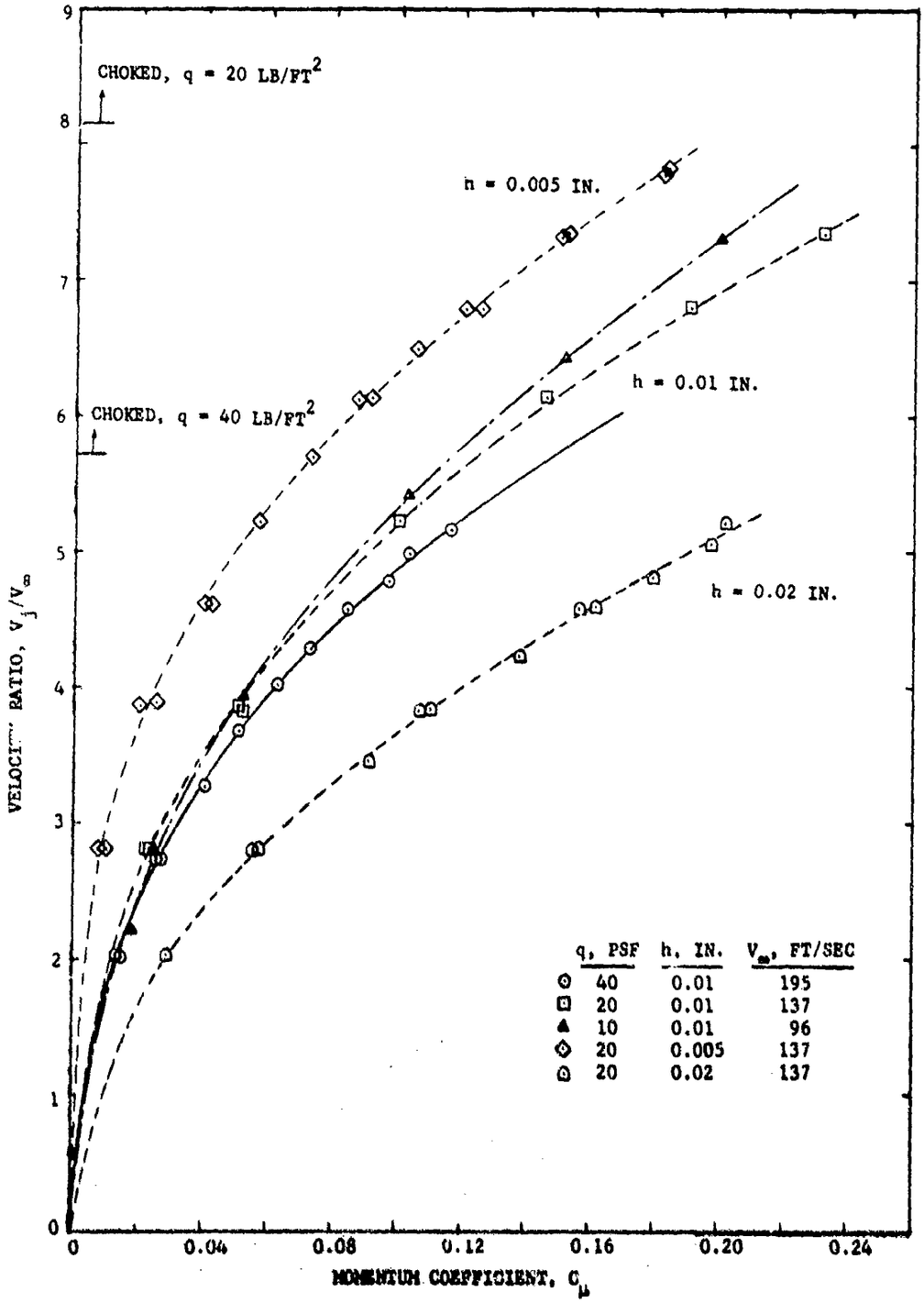

Figure 5 - Experimental Variation of Velocity Ratio with Momentum Coefficient, Slot Height, and Dynamic Pressure

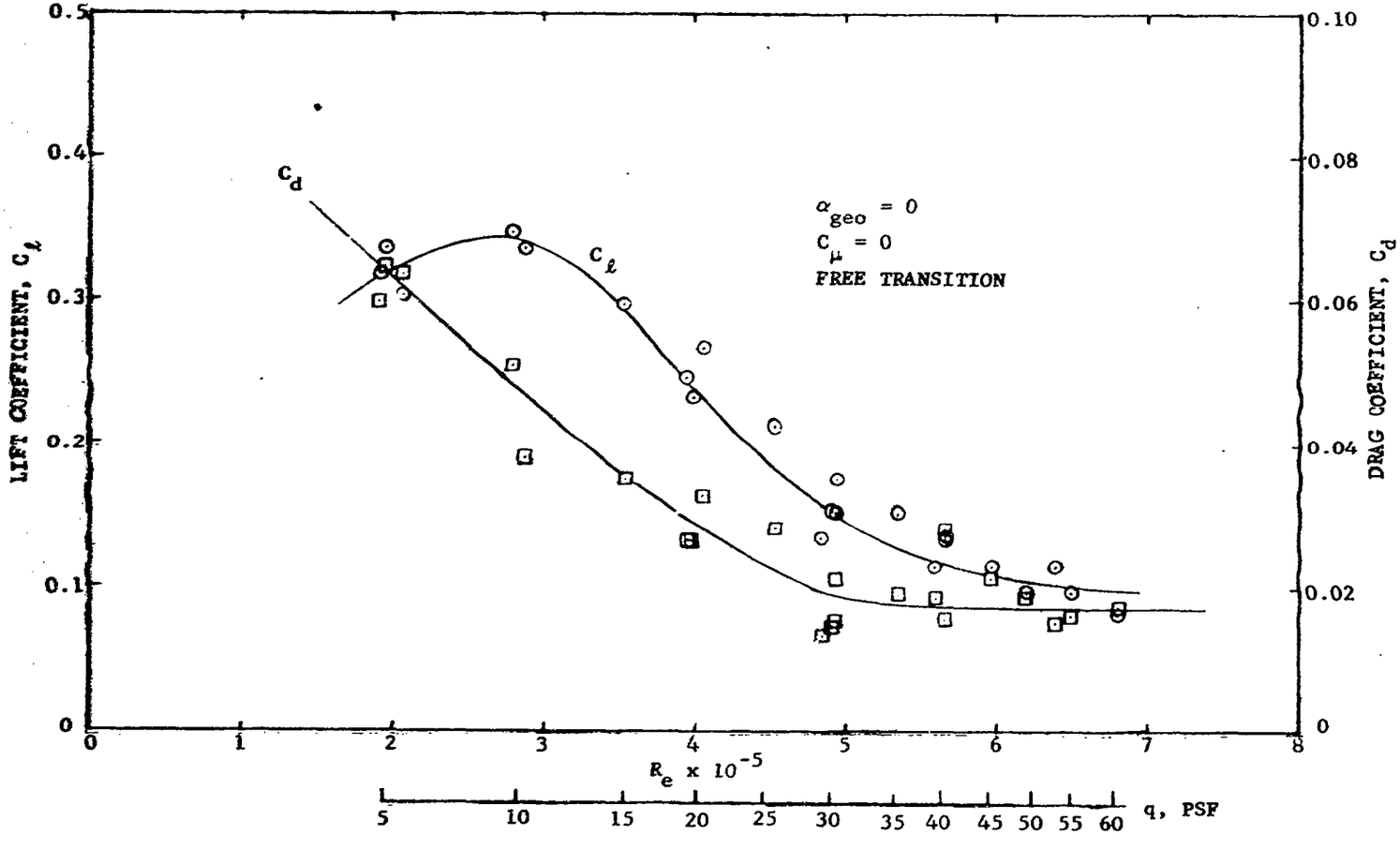

Figure 6 - Variation of Lift and Drag Coefficients with Reynolds Number for the Unblown Ellipse

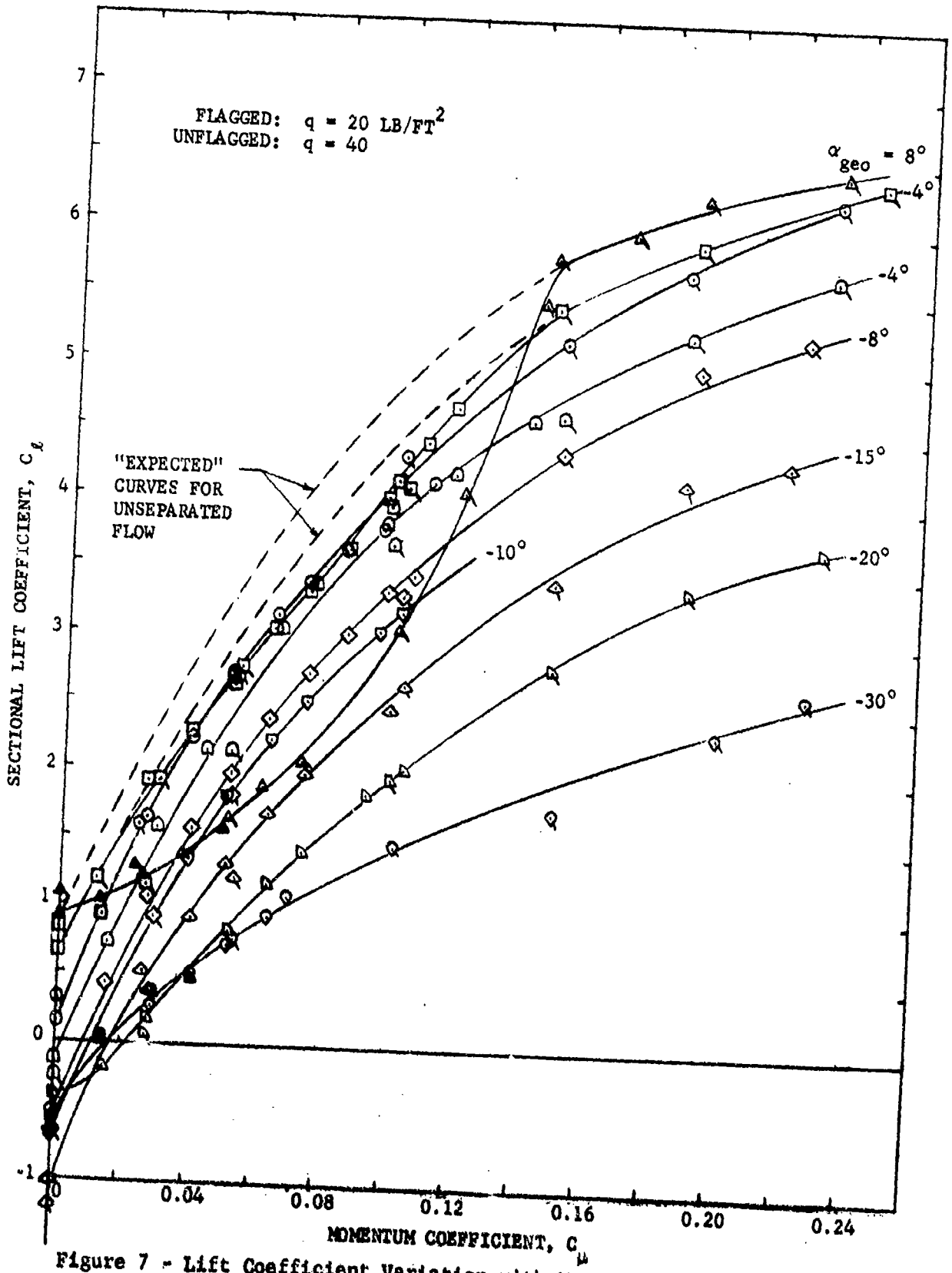

Figure 7 - Lift Coefficient Variation with Momentum Coefficient, h = 0.01 Inch

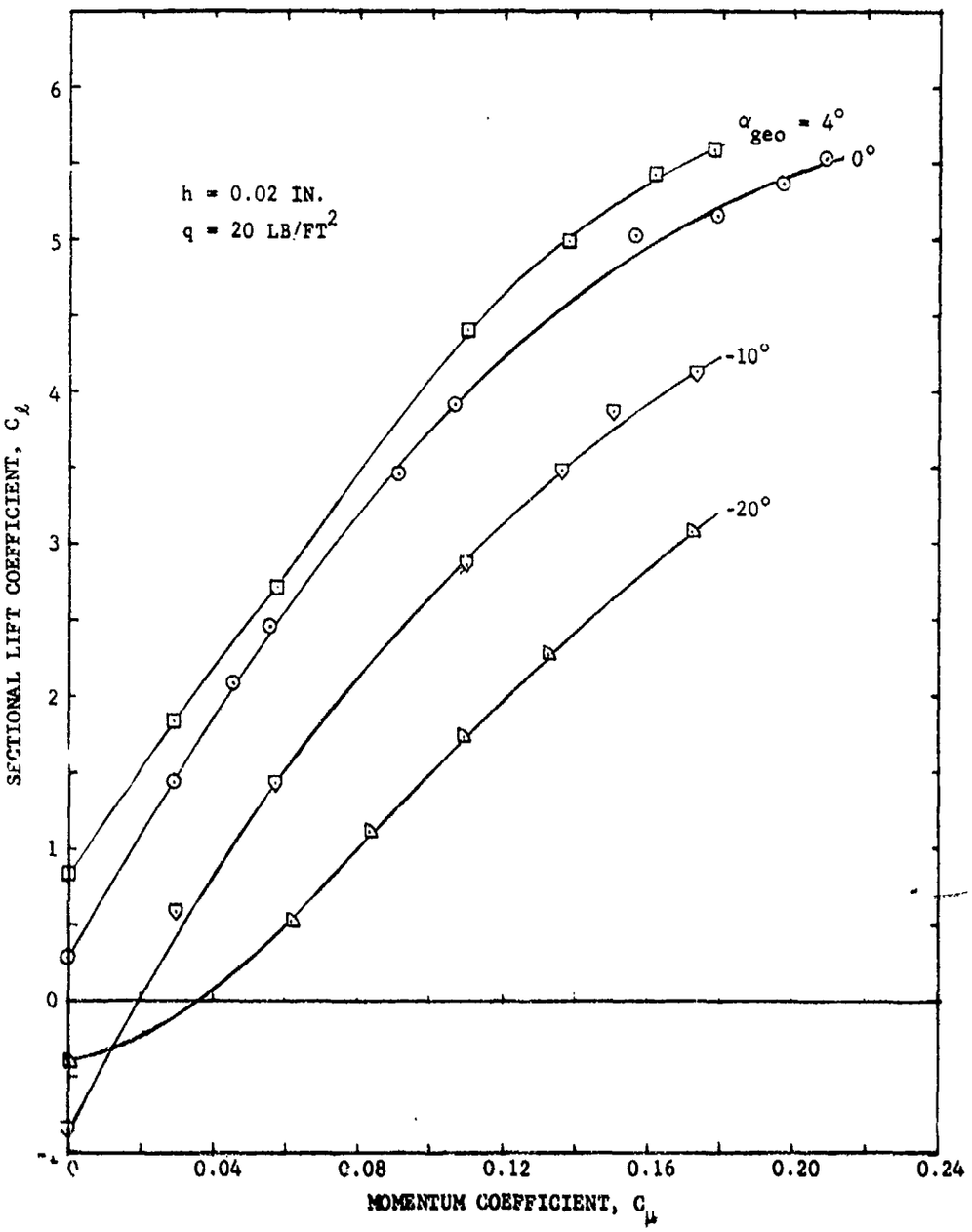

Figure 8 - Lift Coefficient Variation with Momentum Coefficient, h = 0.02 Inch

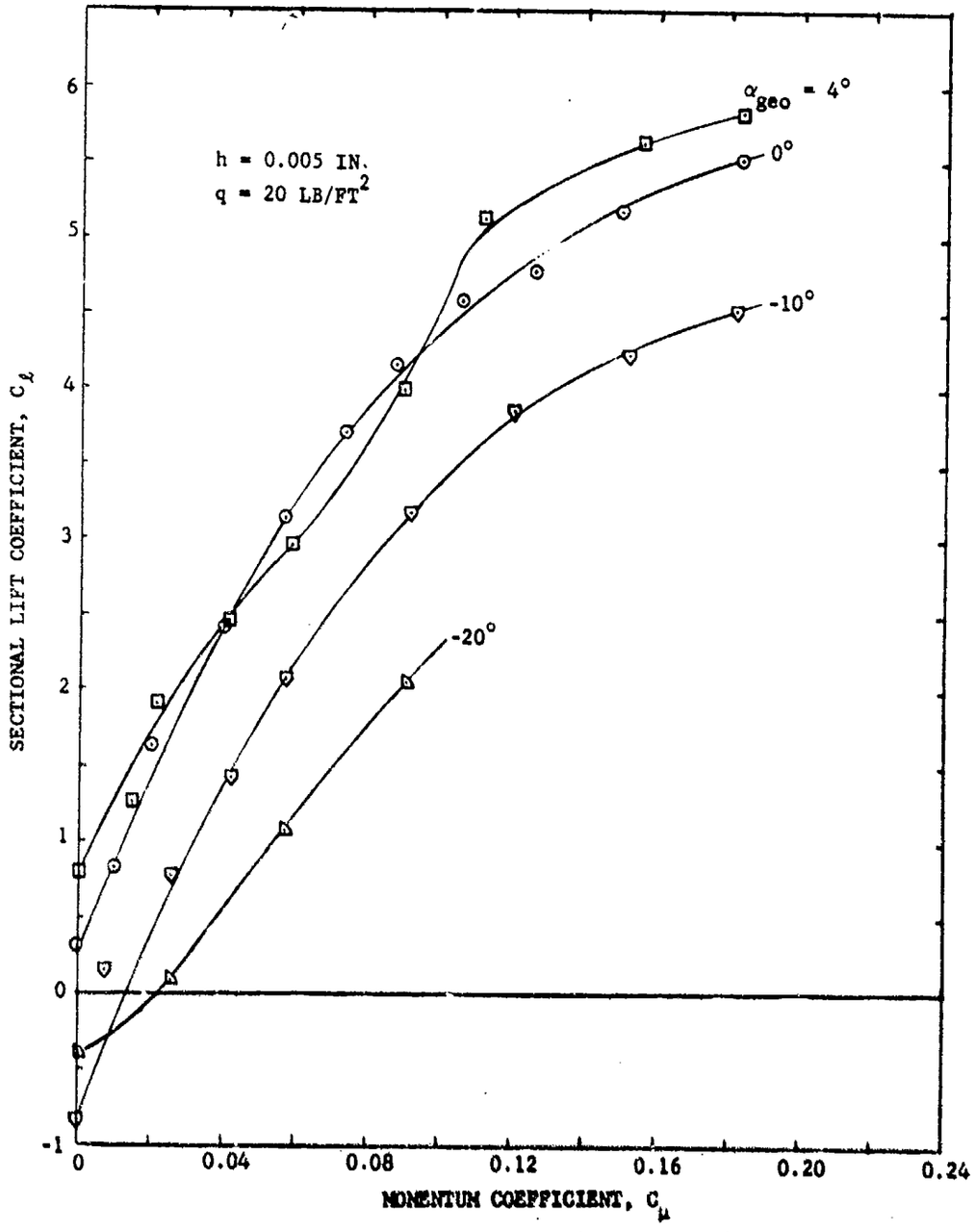

Figure 9 - Lift Coefficient Variation with Momentum Coefficient, h = 0.005 Inch

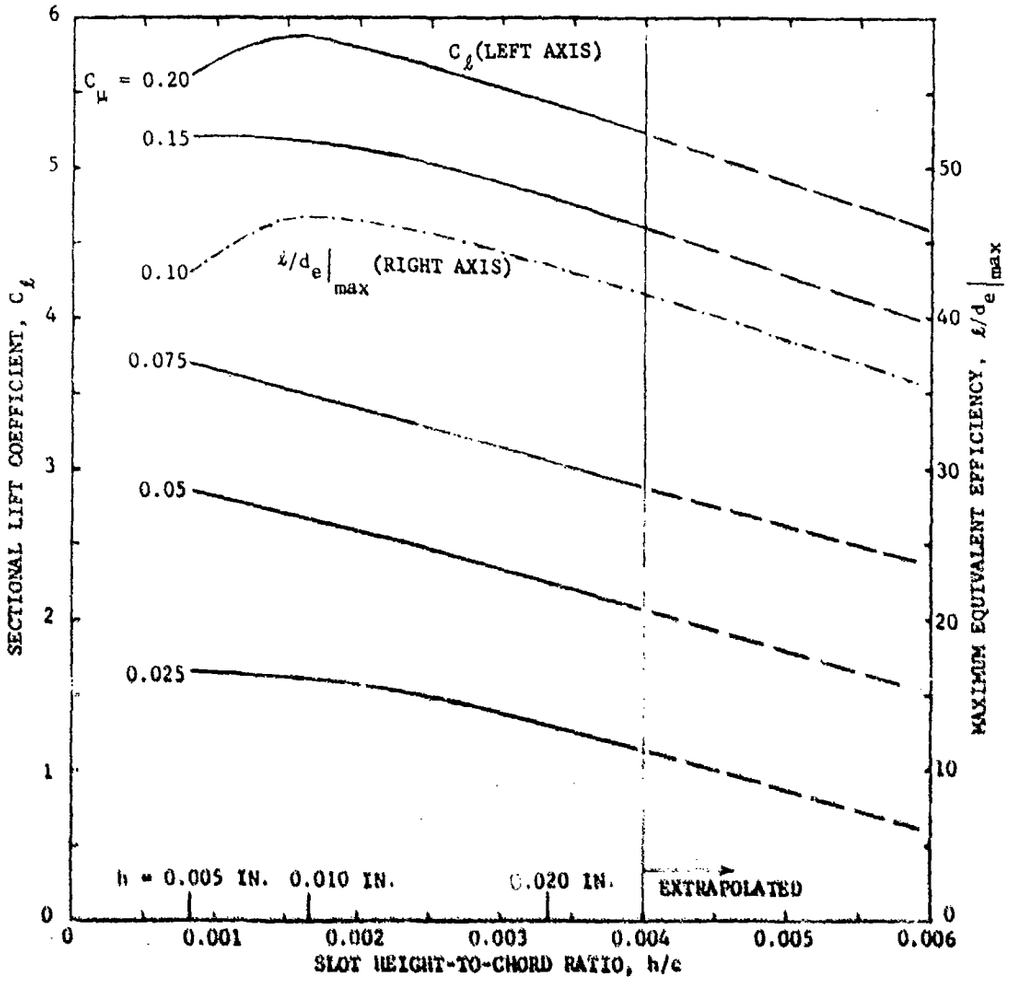

Figure 10 - Effect of Varying Slot Height on Lift and Maximum Equivalent Efficiency at Constant Momentum Coefficient

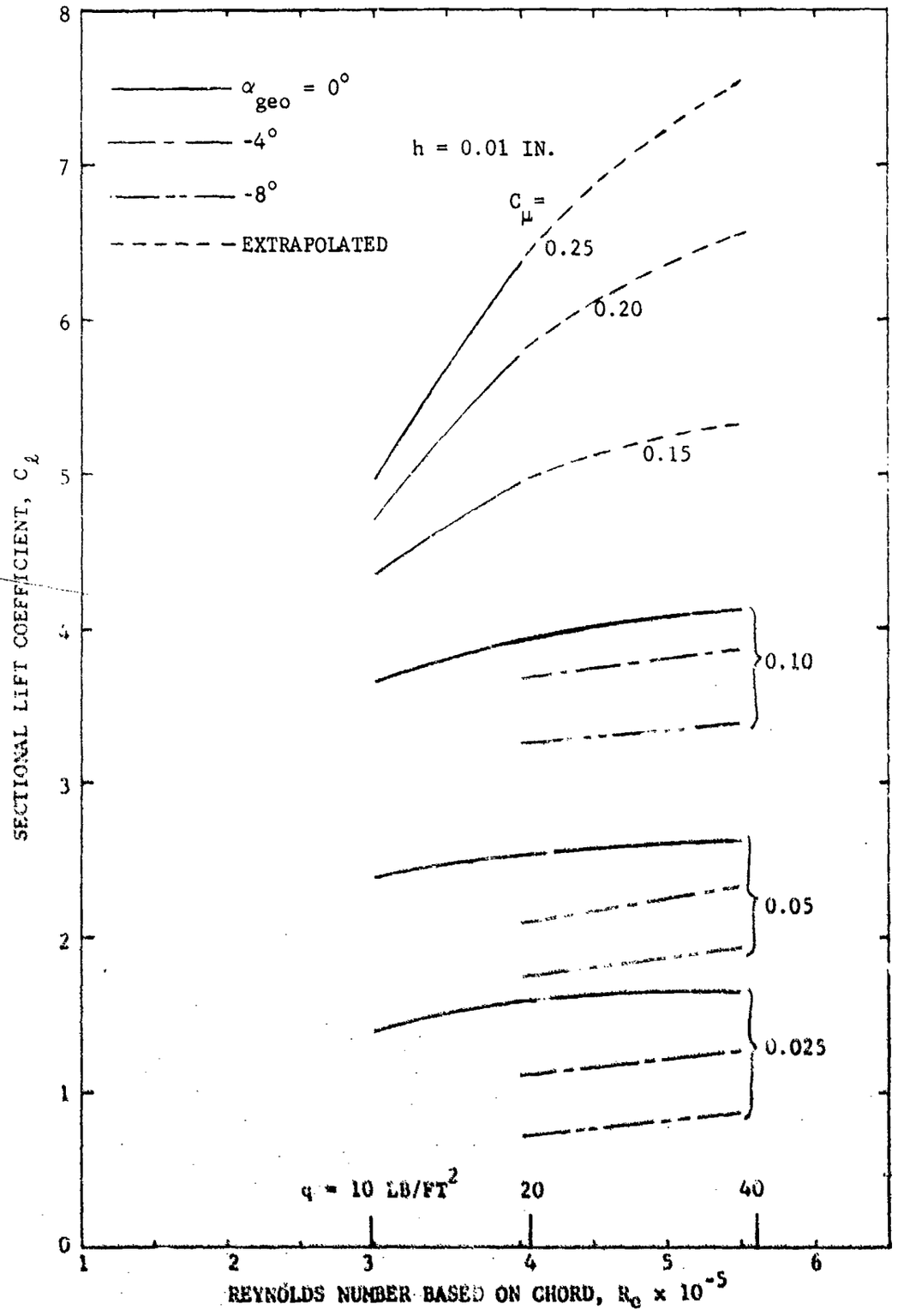

Figure 11 - Reynolds Number Effect on Section Lift Coefficient

$q = 10\ LB/FT^2$

$R_e = 298{,}000$

$V = 96\ FT/SEC$

$h = 0.01\ IN.$

$\alpha_{geo} = 0°$

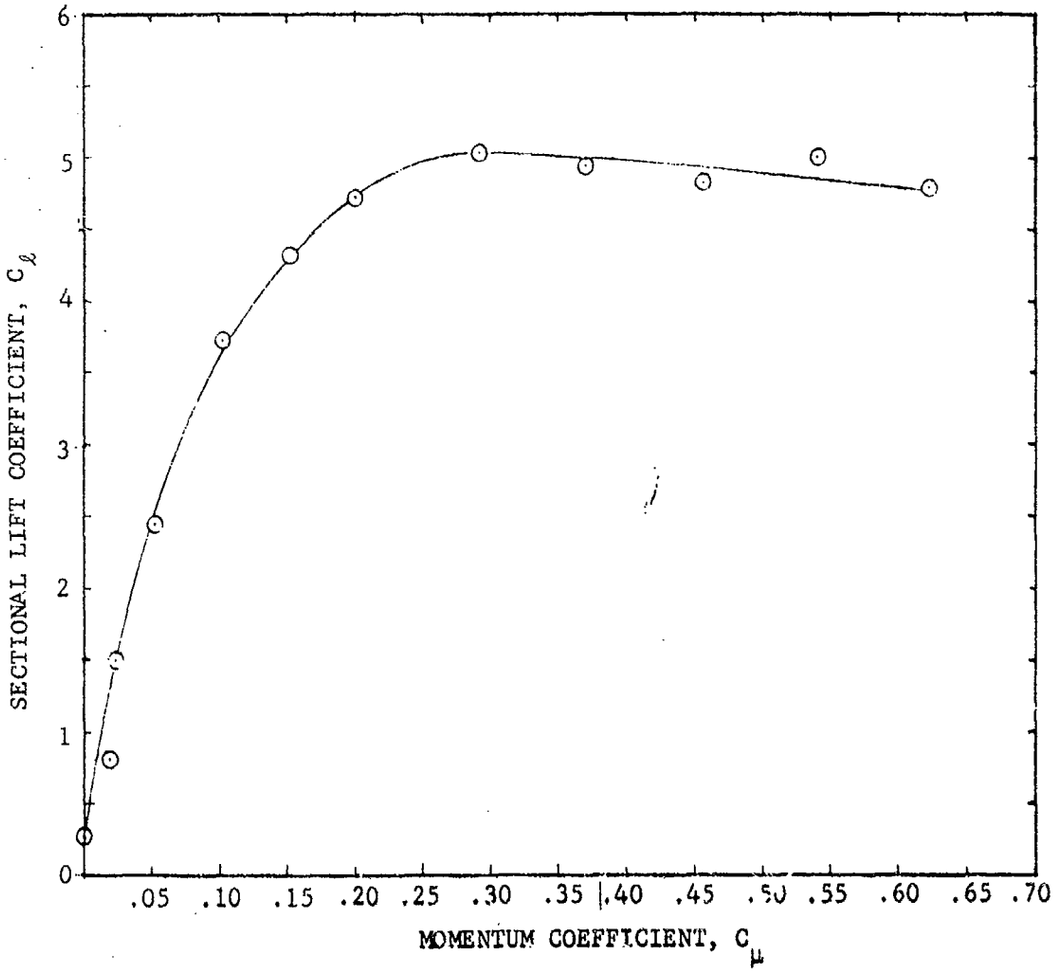

Figure 12 - Lift Variation with Momentum Coefficient for Low Reynolds Number

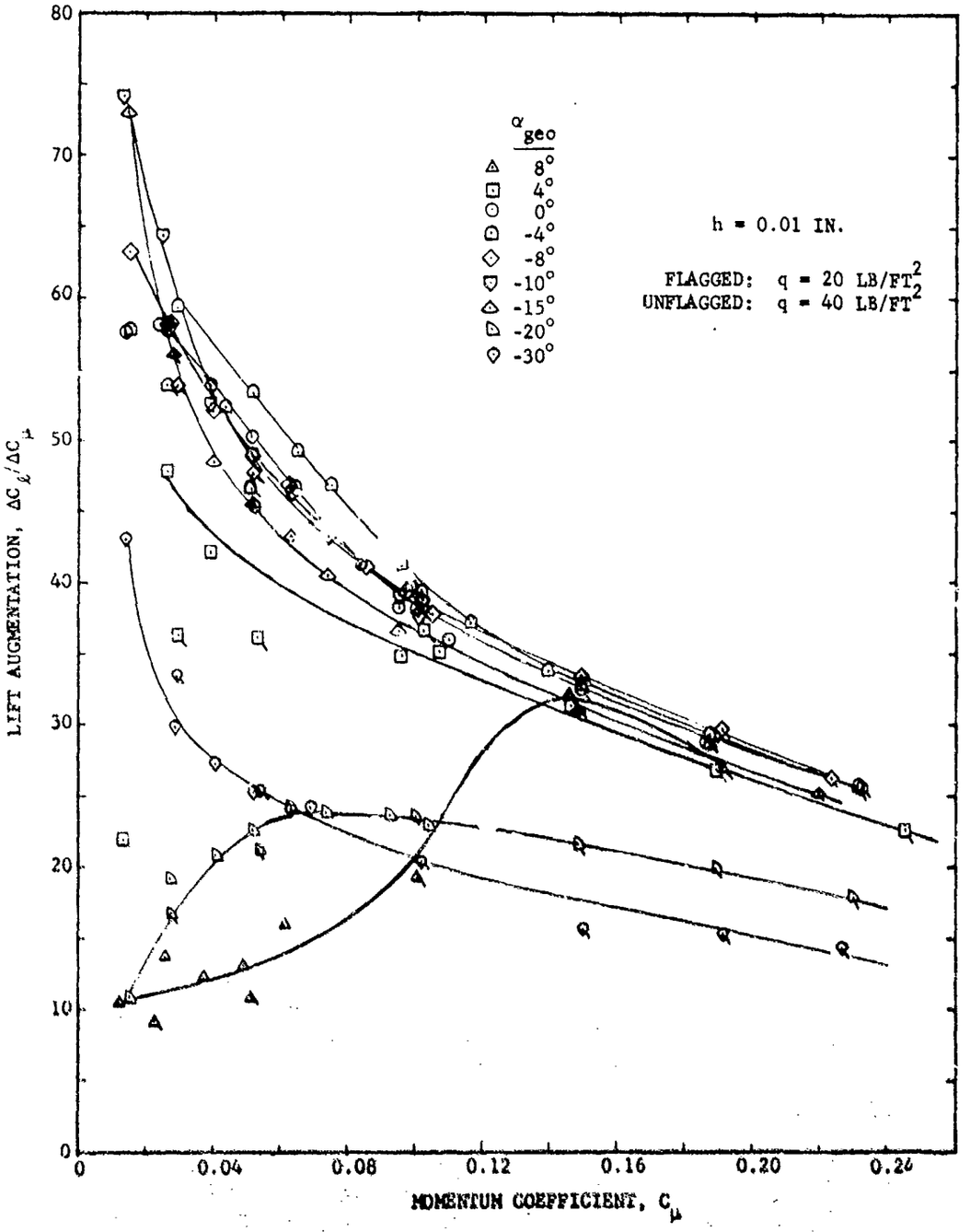

Figure 13 - Lift Augmentation, h = 0.01 Inch

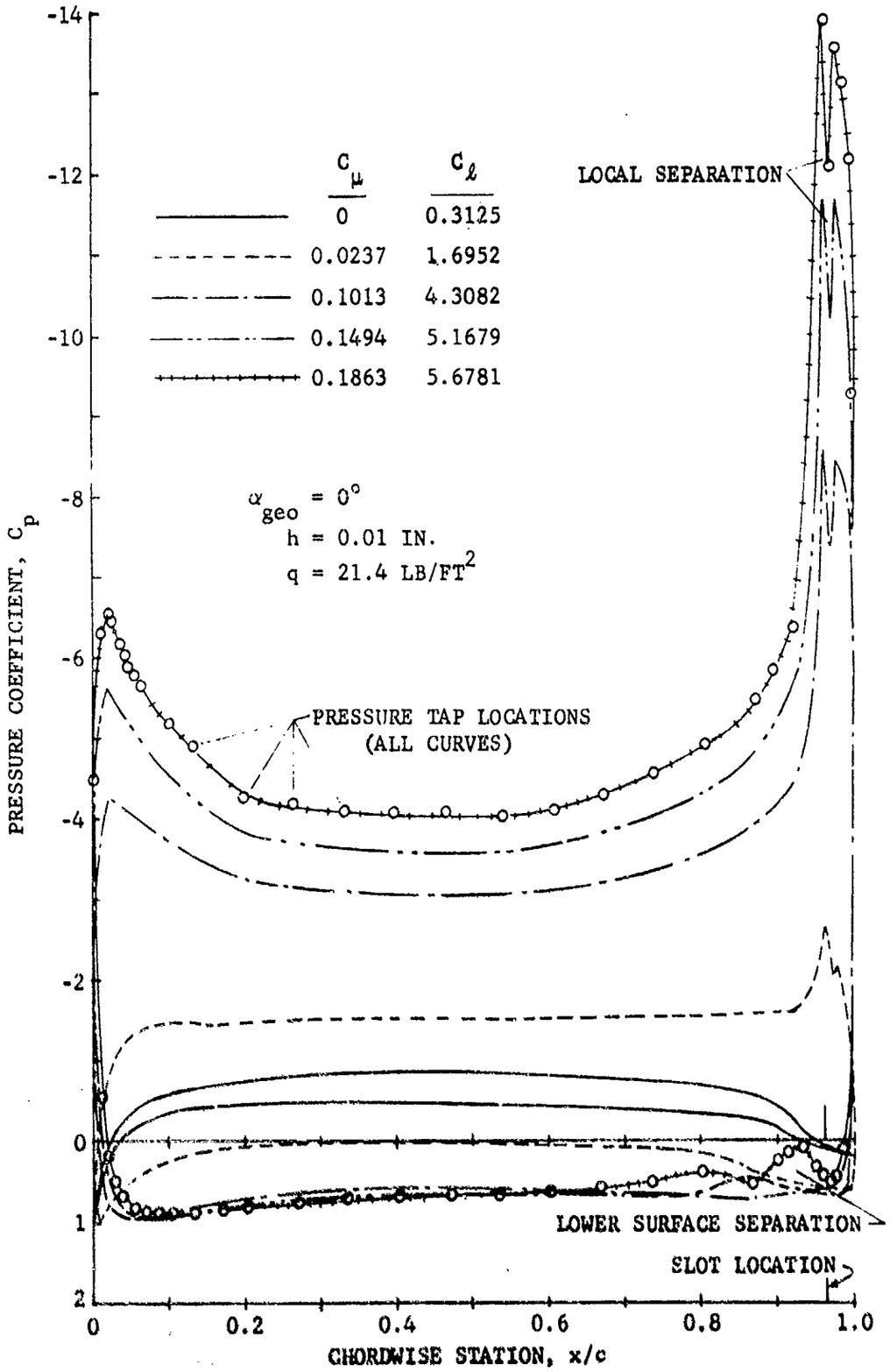

Figure 14 - Experimental Pressure Distributions at Zero Geometric Incidence (α_{geo} = 0°)

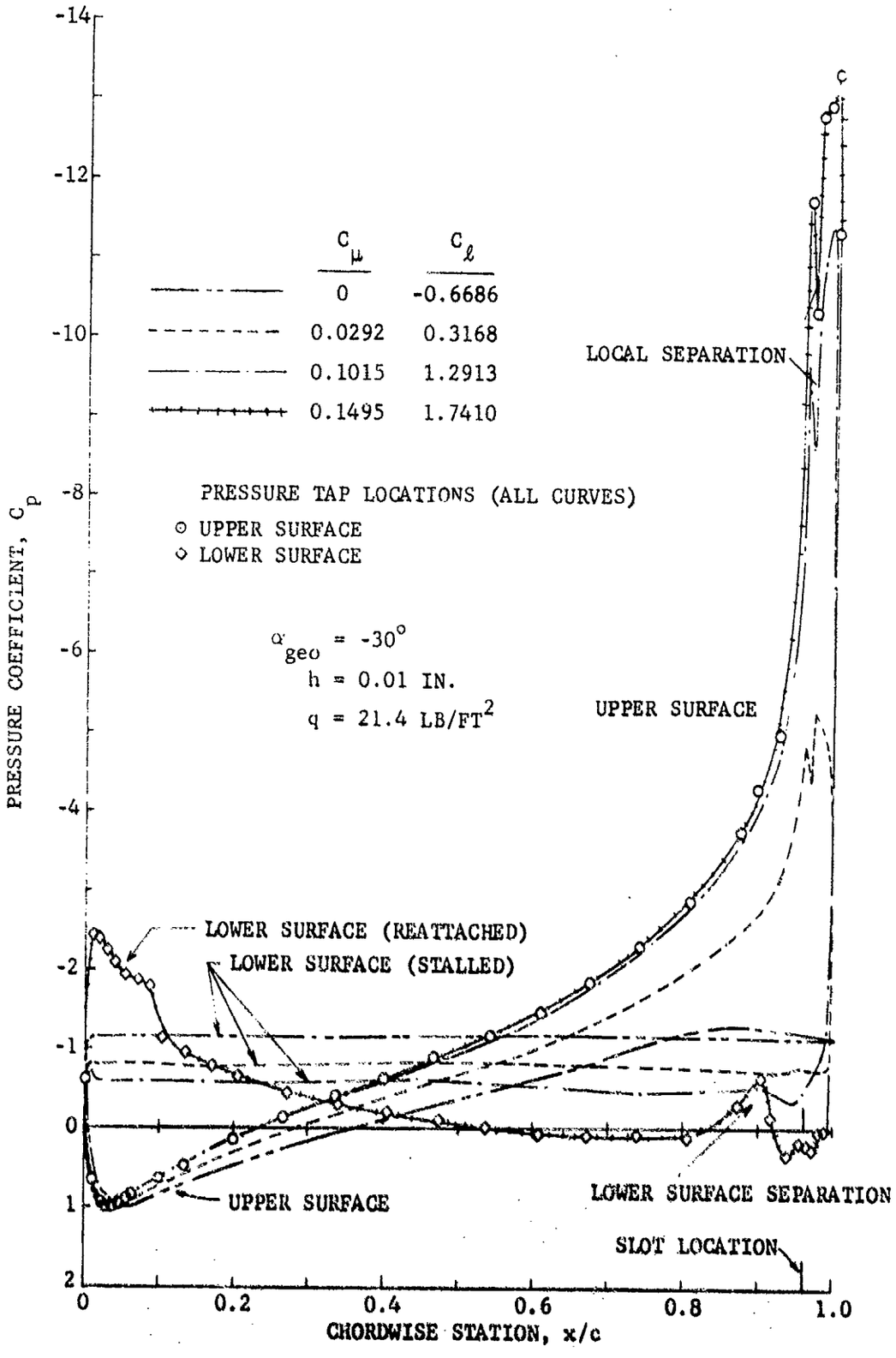

Figure 15 - Experimental Pressure Distributions at Large Negative Incidence (α_{geo} = -30°)

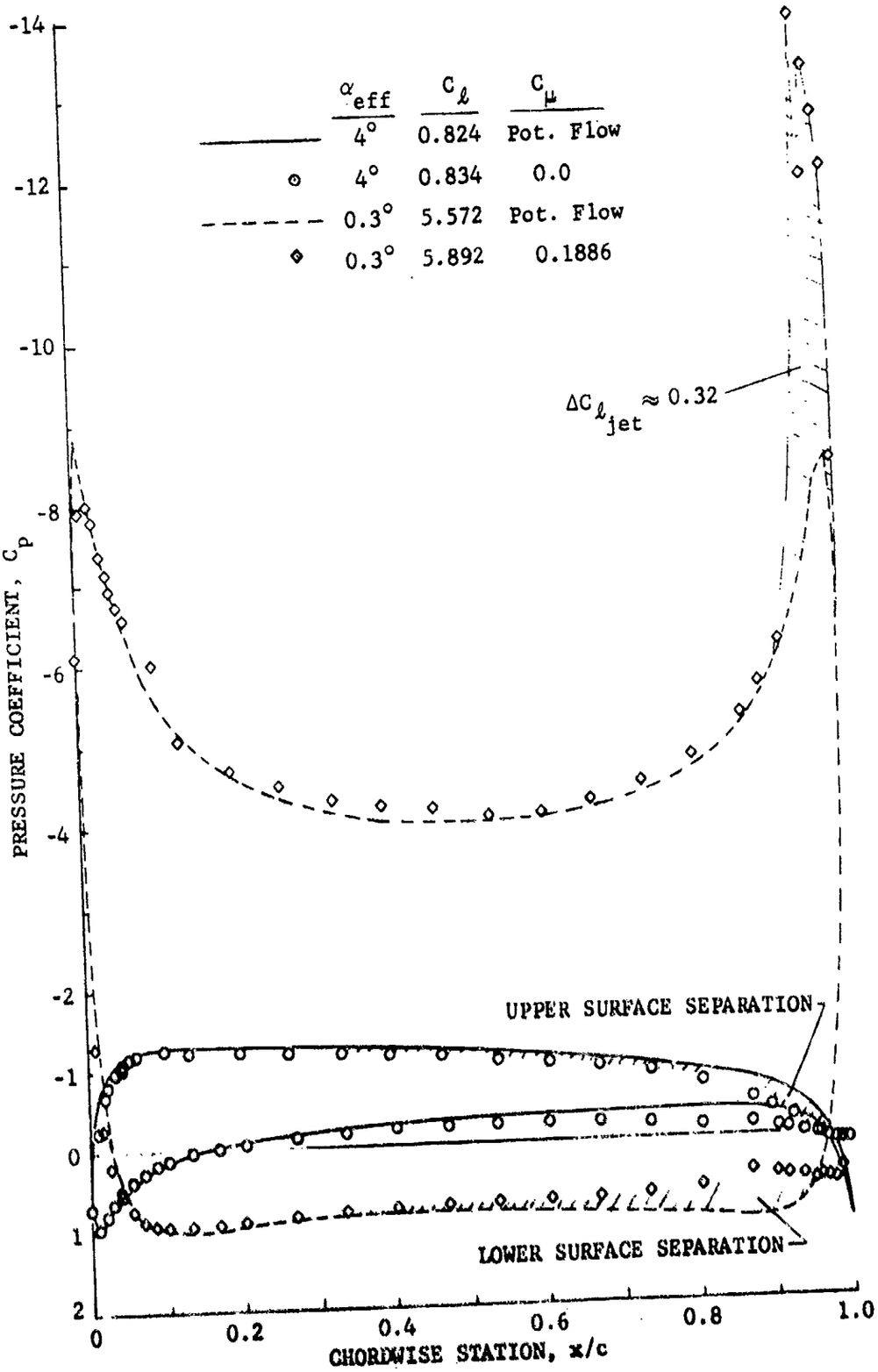

Figure 16 - Comparison of Potential Flow and Experimental Pressure Distributions ($\alpha_{geo} = 4°$)

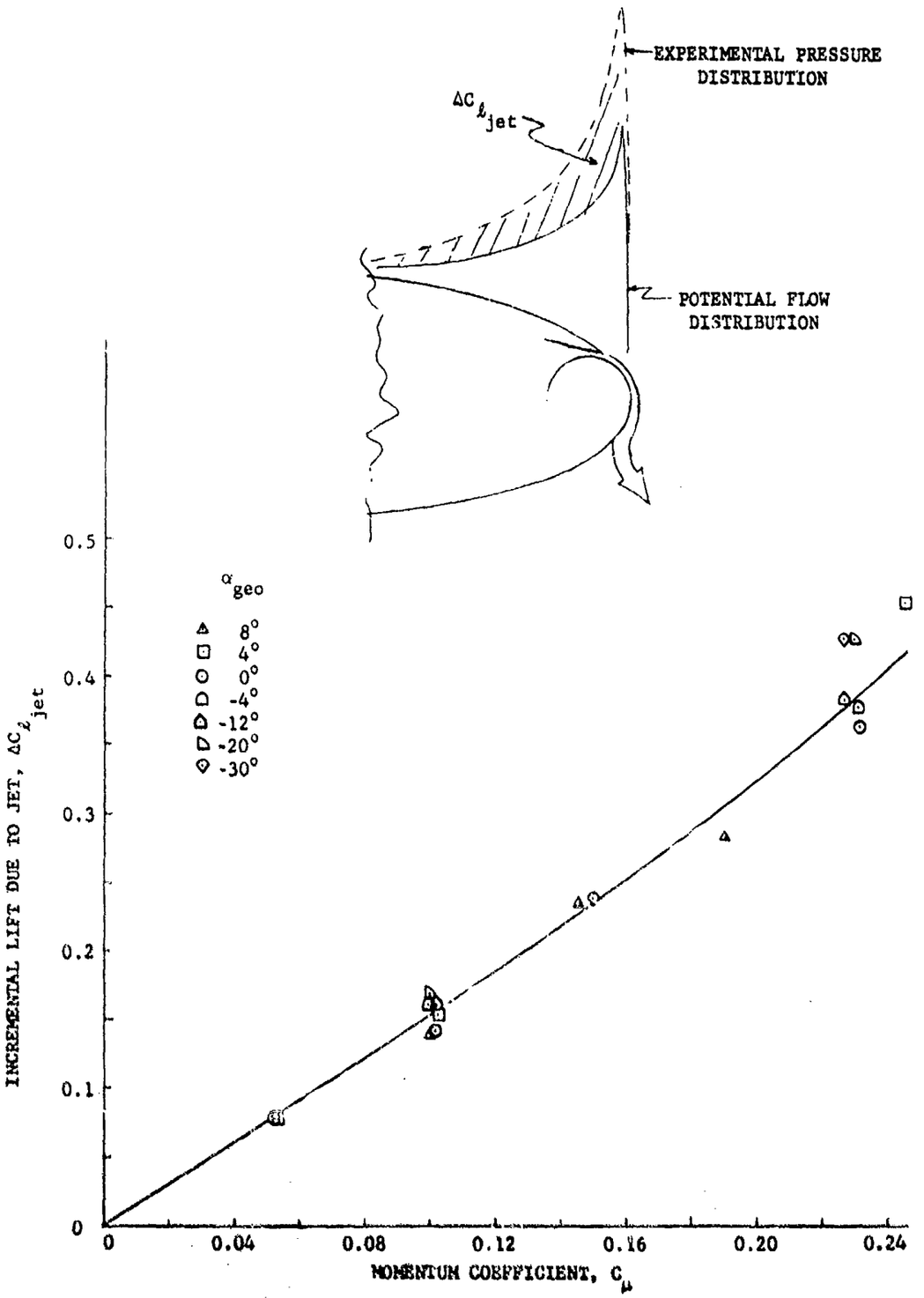

Figure 17 - Incremental Lift Coefficient Due to Suction in the Trailing Edge Jet

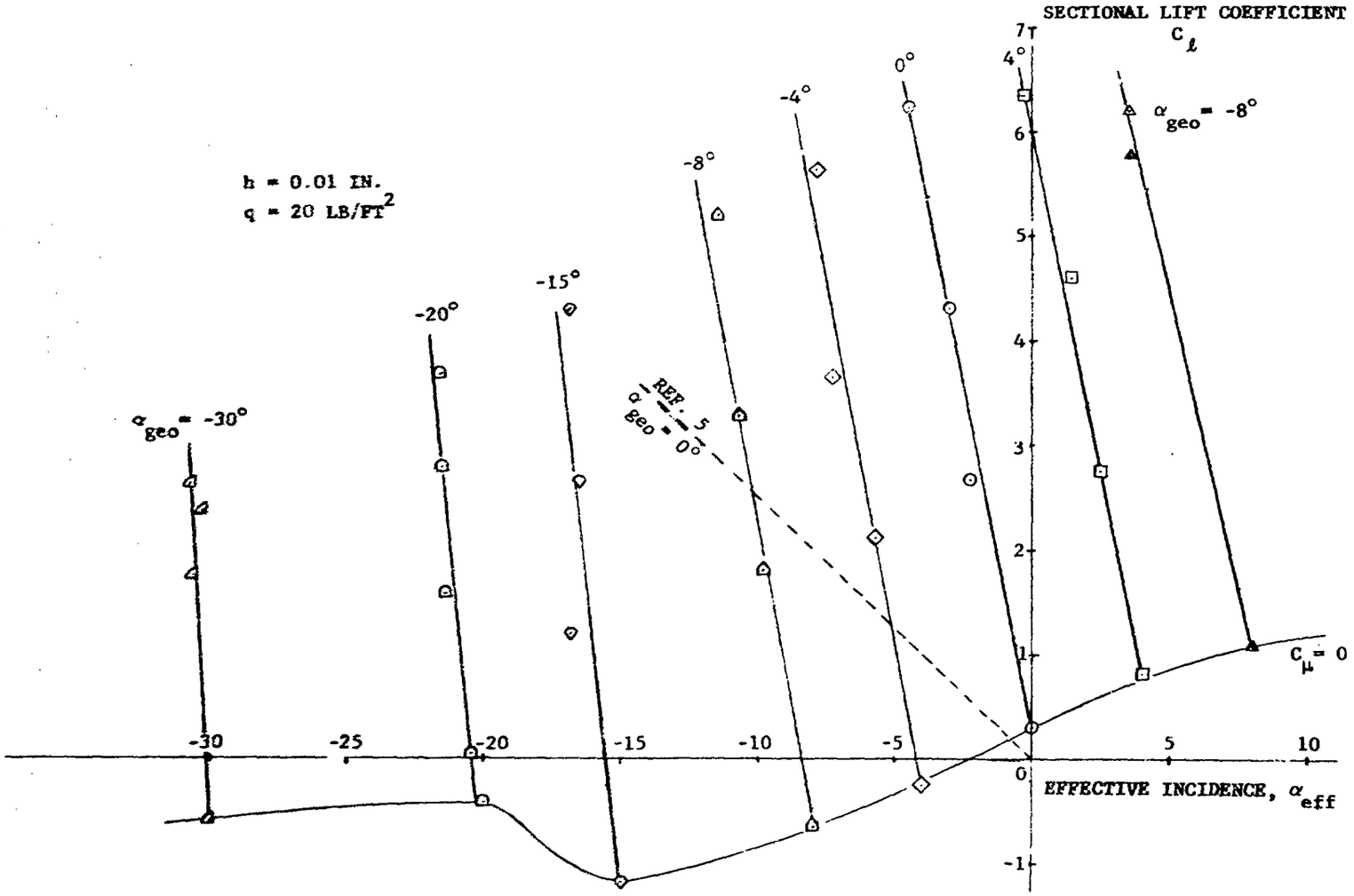

Figure 18 - Induced Angle (Downwash) Corrections to Geometric Incidence

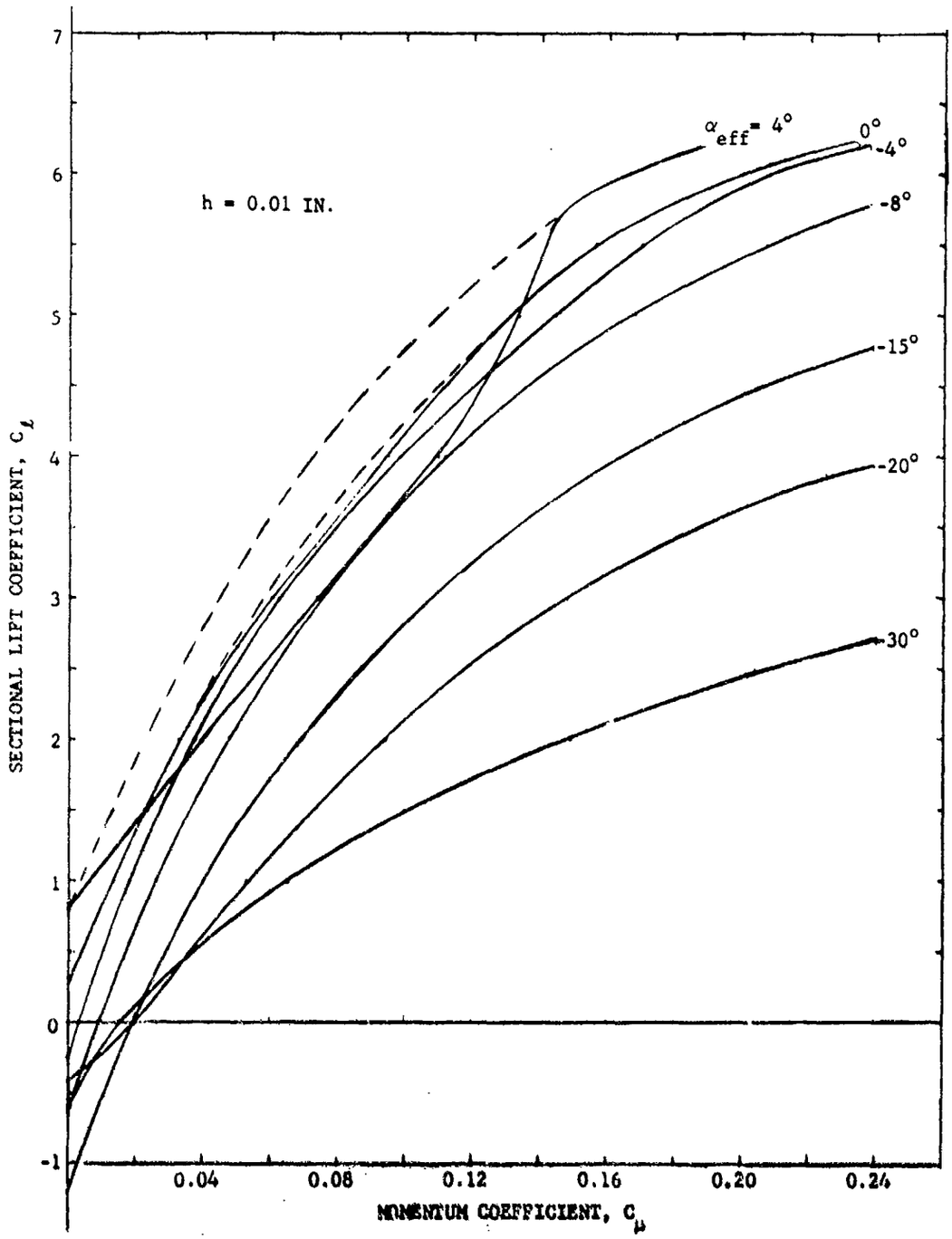

Figure 19 - Lift Variation with Momentum Coefficient at Constant Effective Incidence

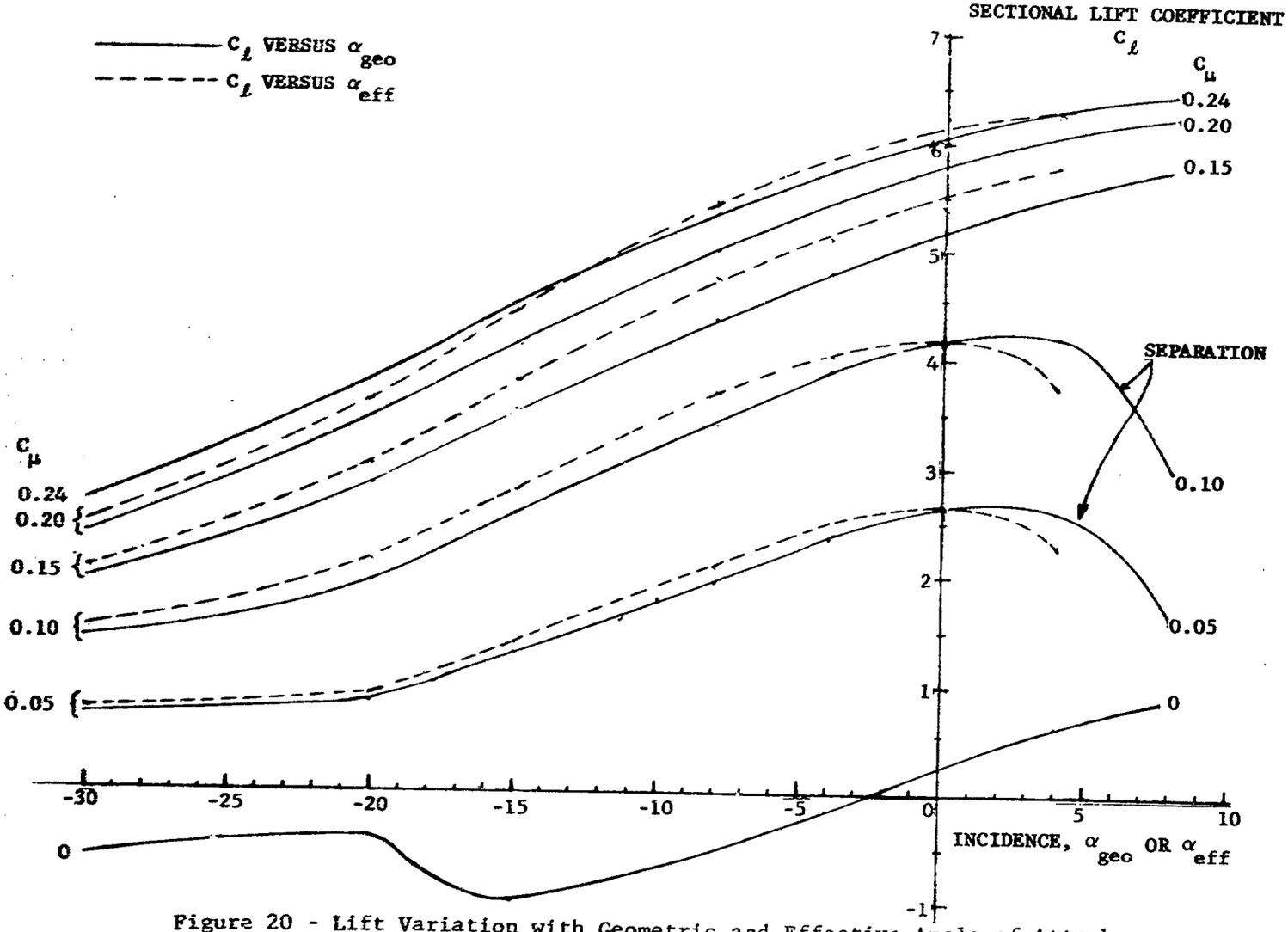

Figure 20 - Lift Variation with Geometric and Effective Angle of Attack

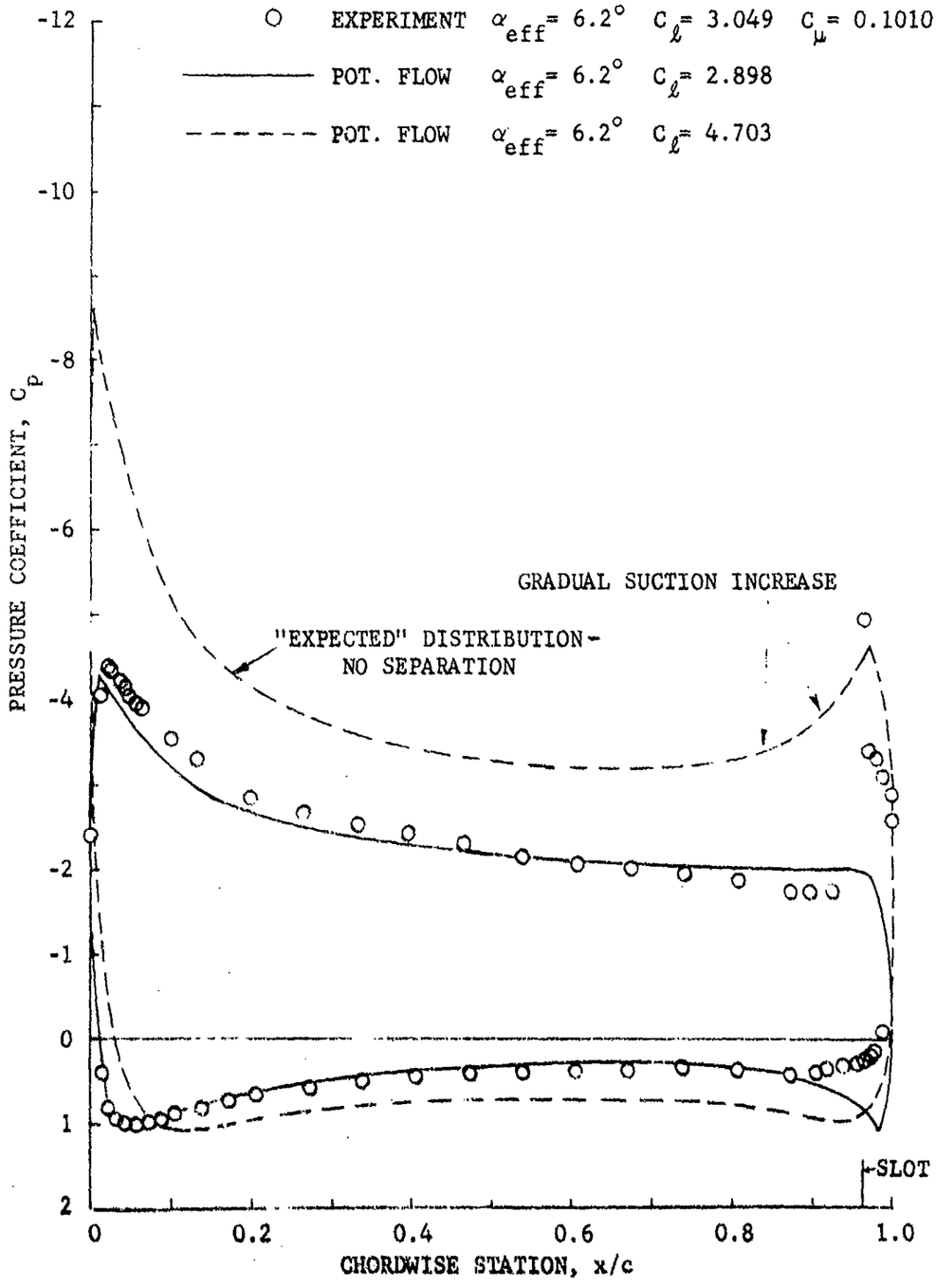

Figure 21 - Pressure Distributions in the Hysteresis (Separated) Region (α_{geo} = 8°)

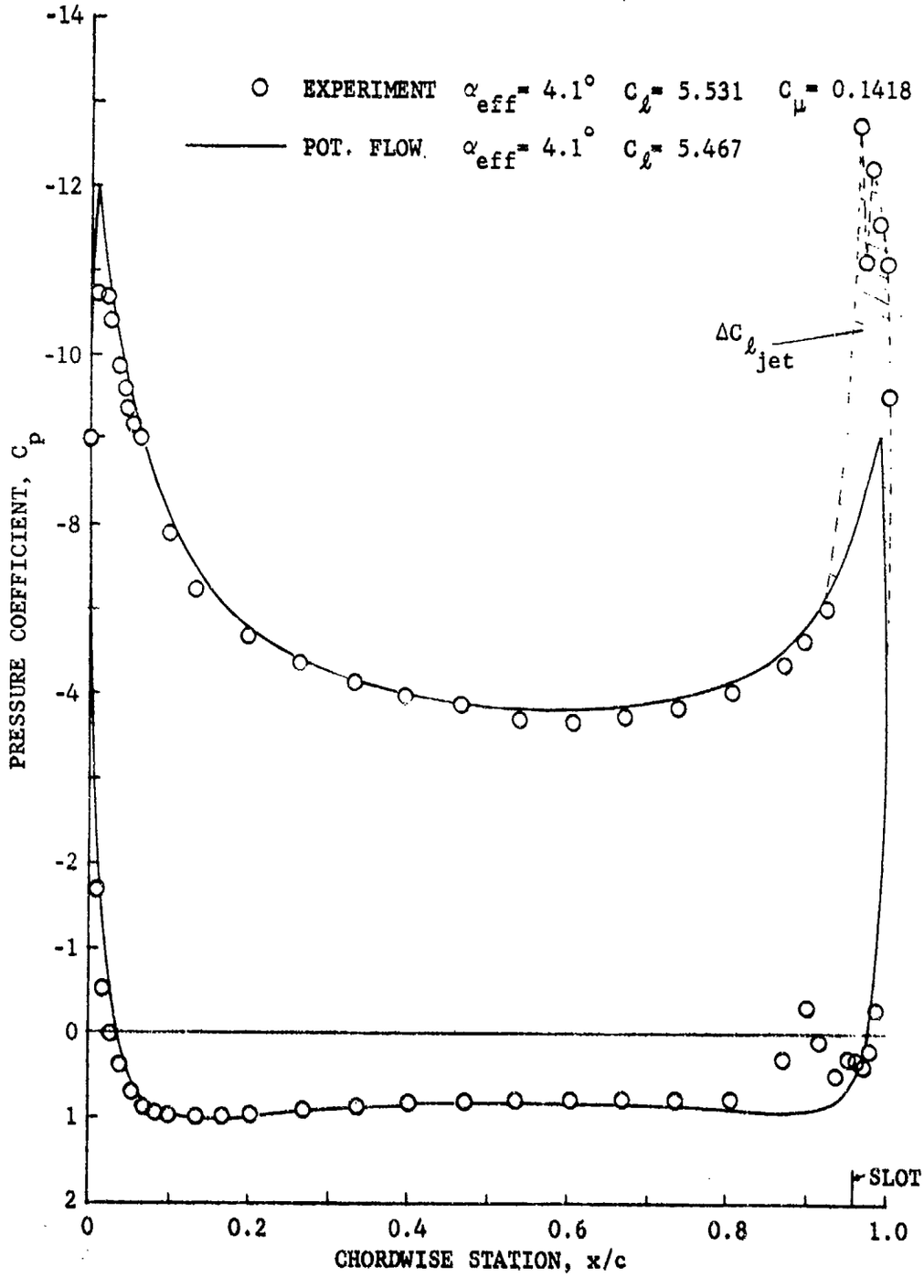

Figure 22 - Pressure Distributions for Reattached Flow (α_{geo} = 8°)

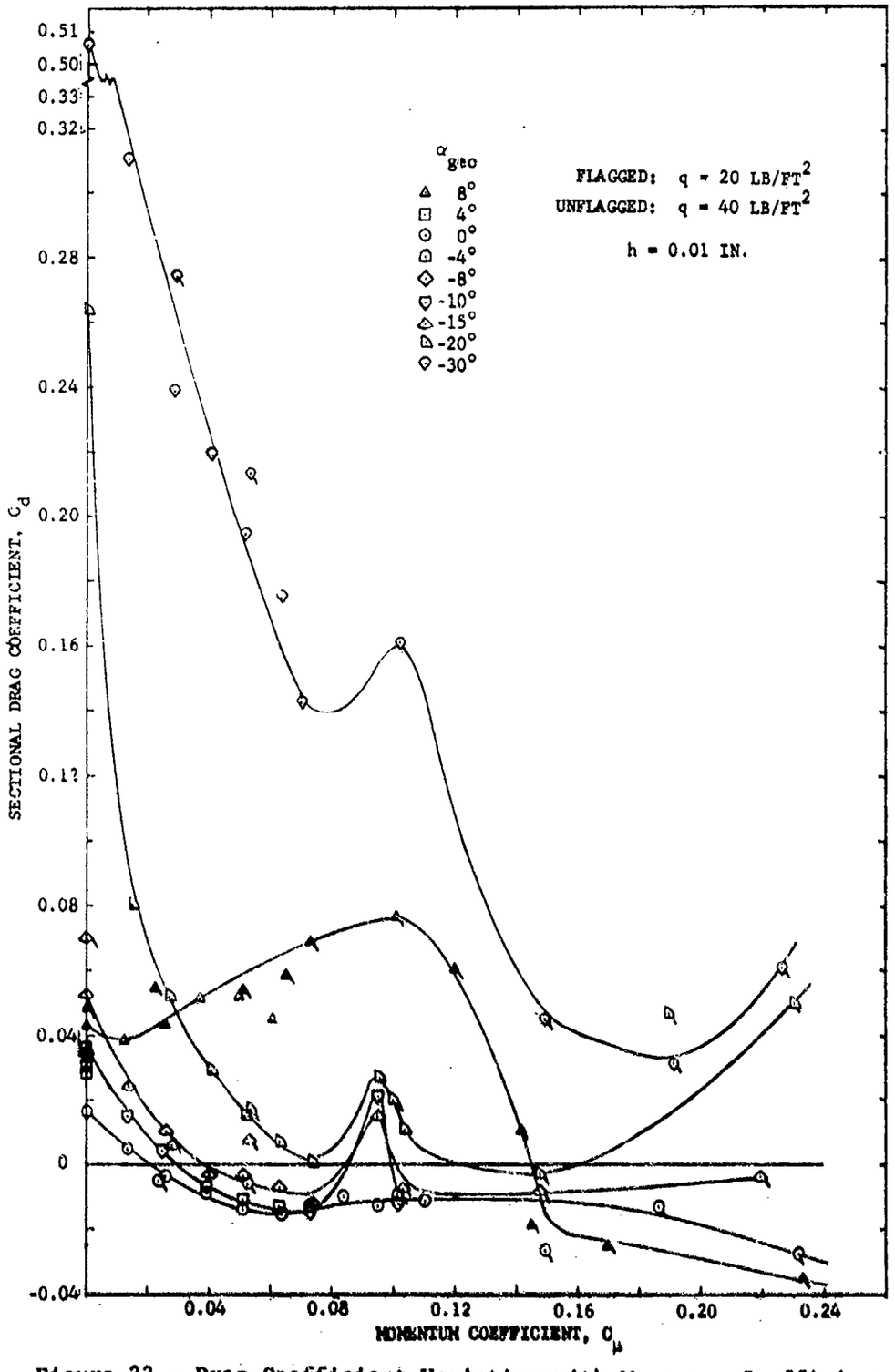

Figure 23 - Drag Coefficient Variation with Momentum Coefficient

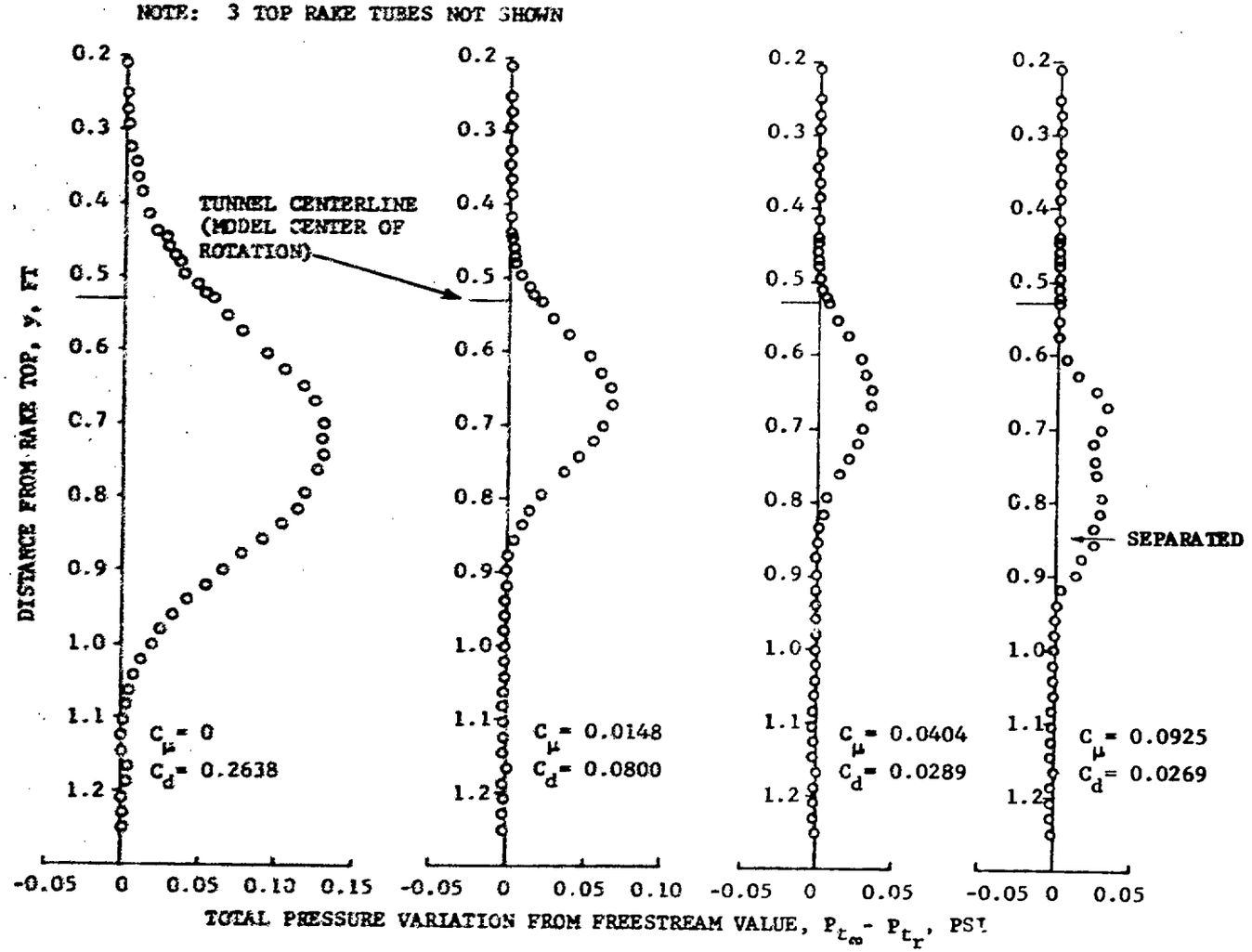

Figure 24 - Wake Rake Total Pressure Distributions for α_{geo} = -20°, h = 0.01 Inch

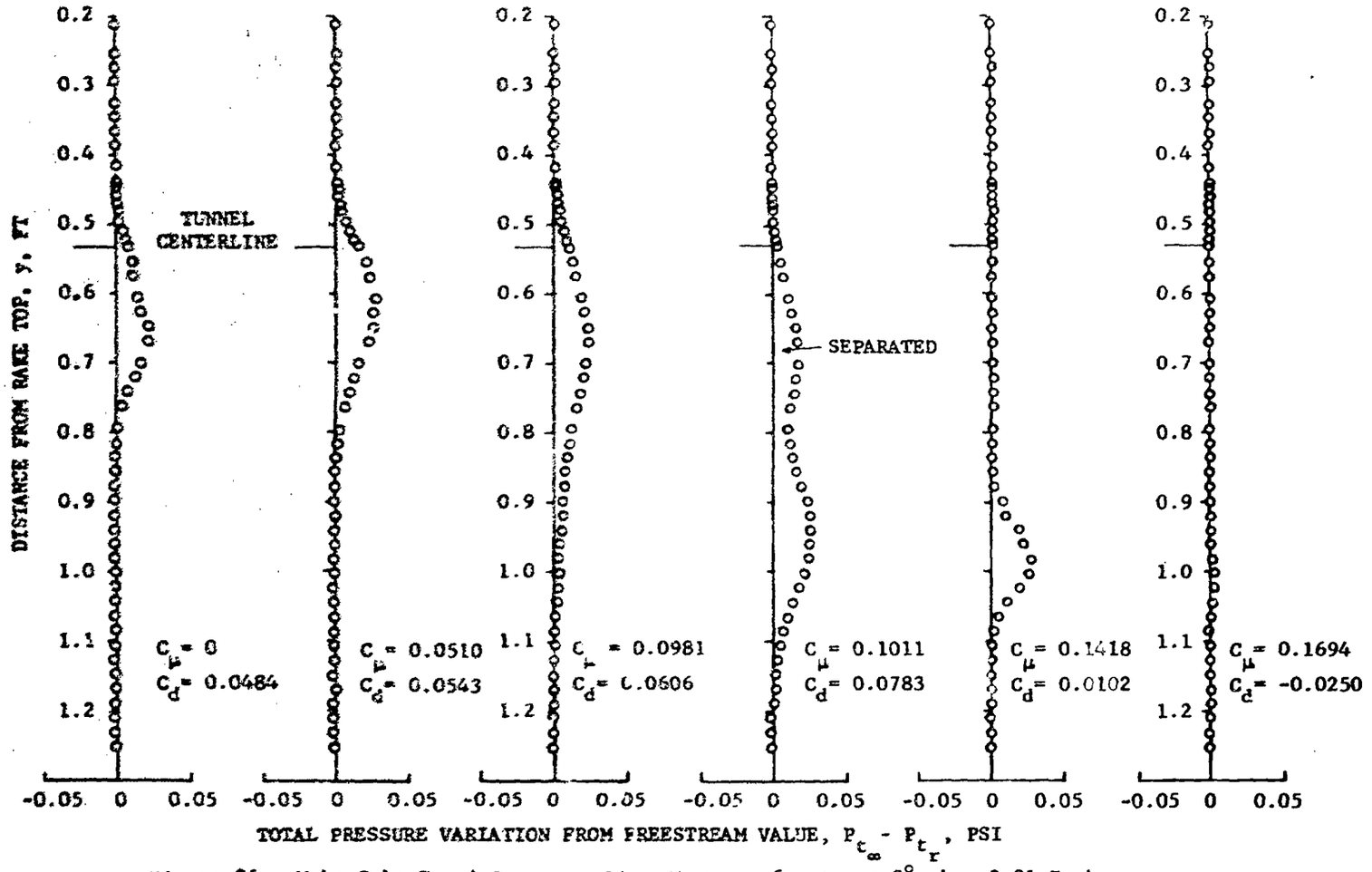

Figure 25 - Wake Rake Total Pressure Distributions for $\alpha_{geo} = 8^\circ$, h = 0.01 Inch

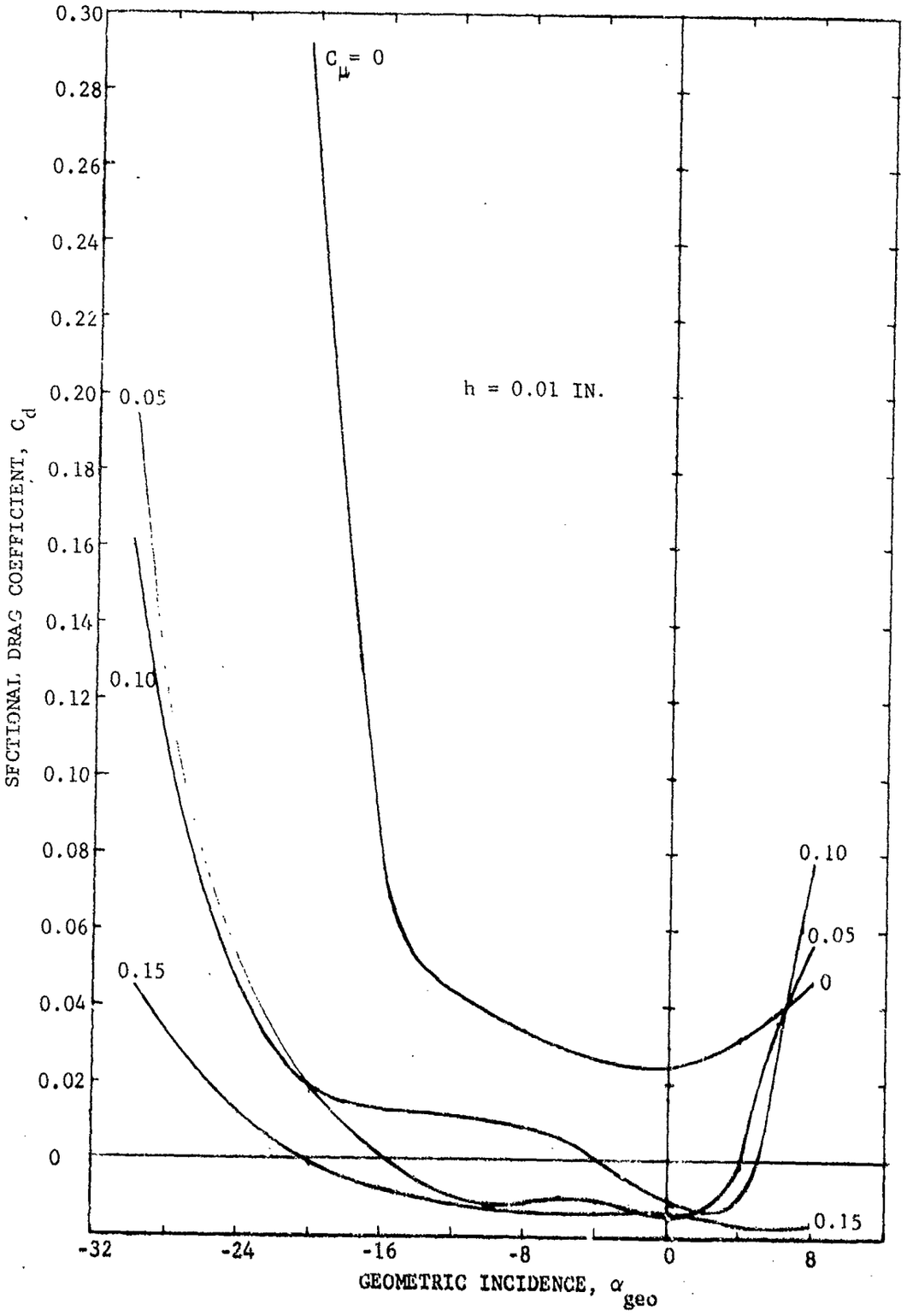

Figure 26 - Drag Variation with Geometric Angle of Attack

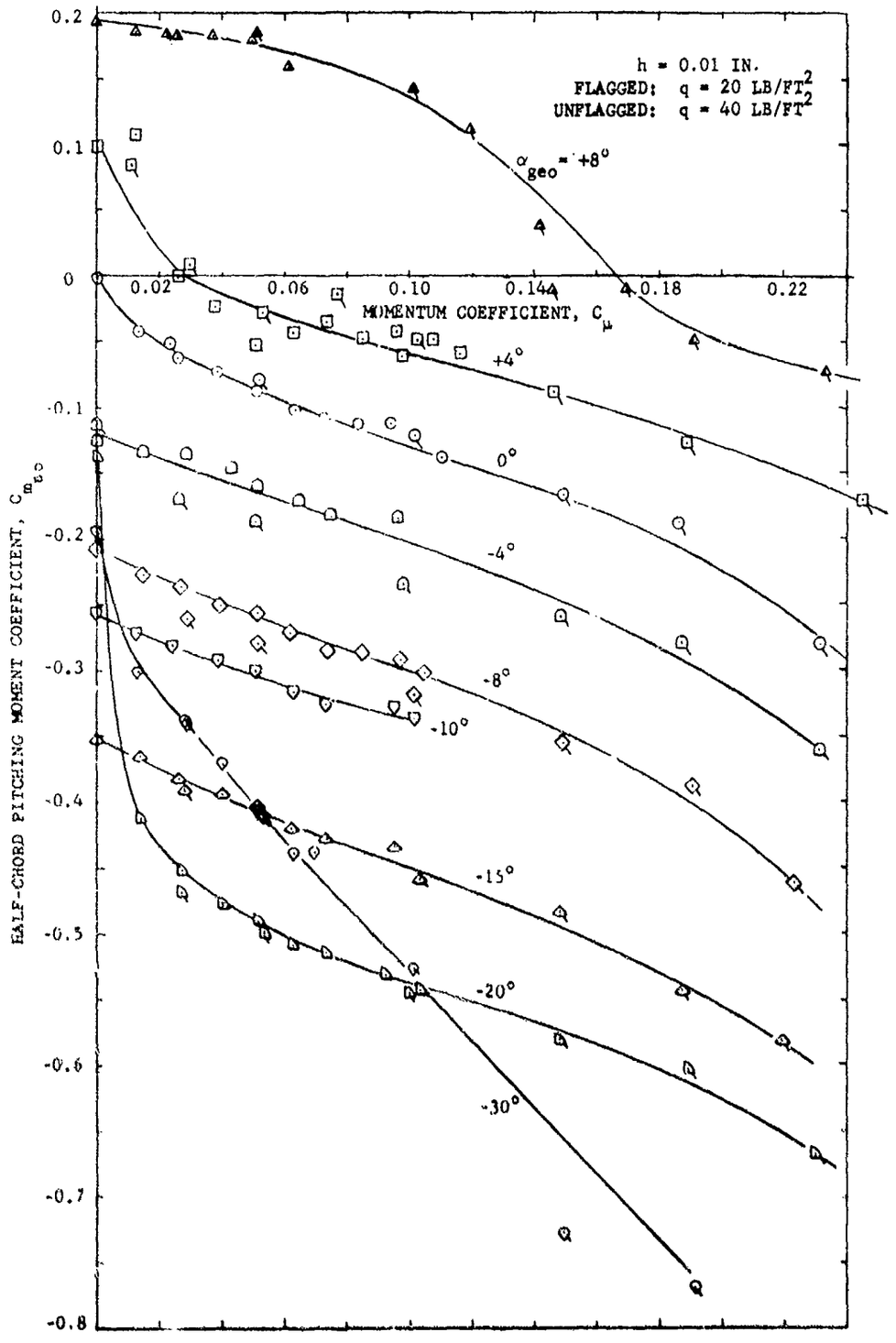

Figure 27 - Variation in Half-Chord Pitching Moment Coefficient

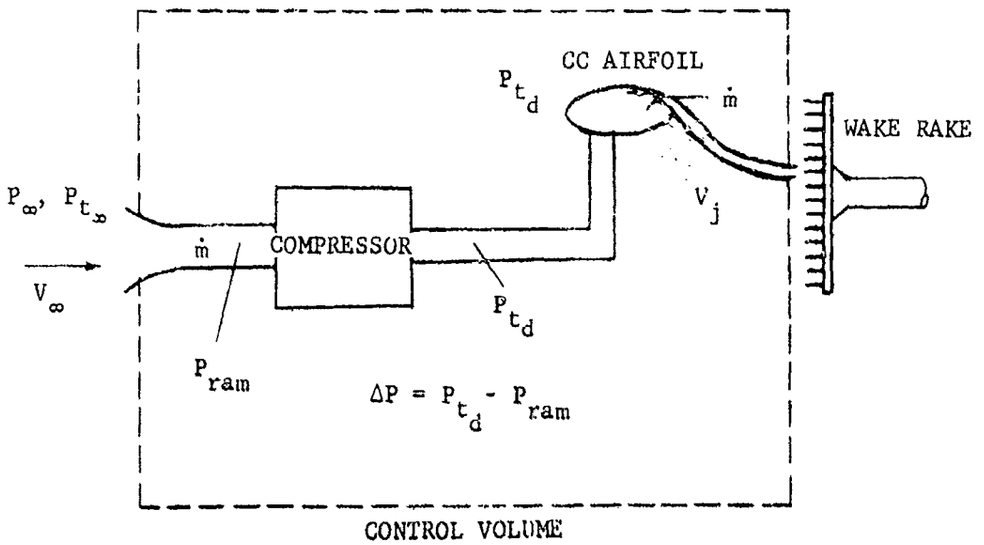

Figure 28 - Schematic for Determination of Equivalent Drag

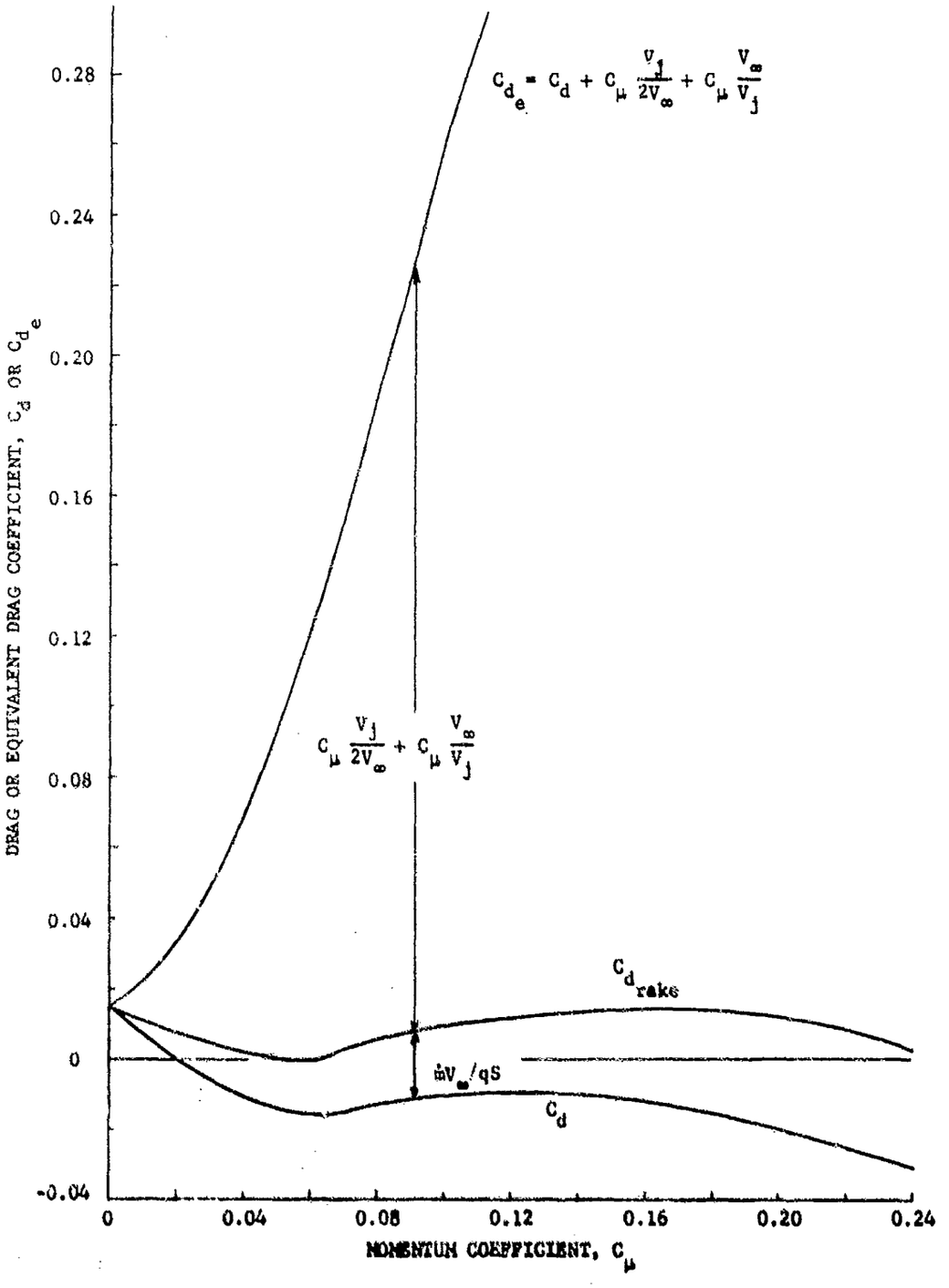

Figure 29 - Comparison of Measured and Equivalent Drag Coefficients ($\alpha_{geo} = 0$, h = 0.01 Inch)

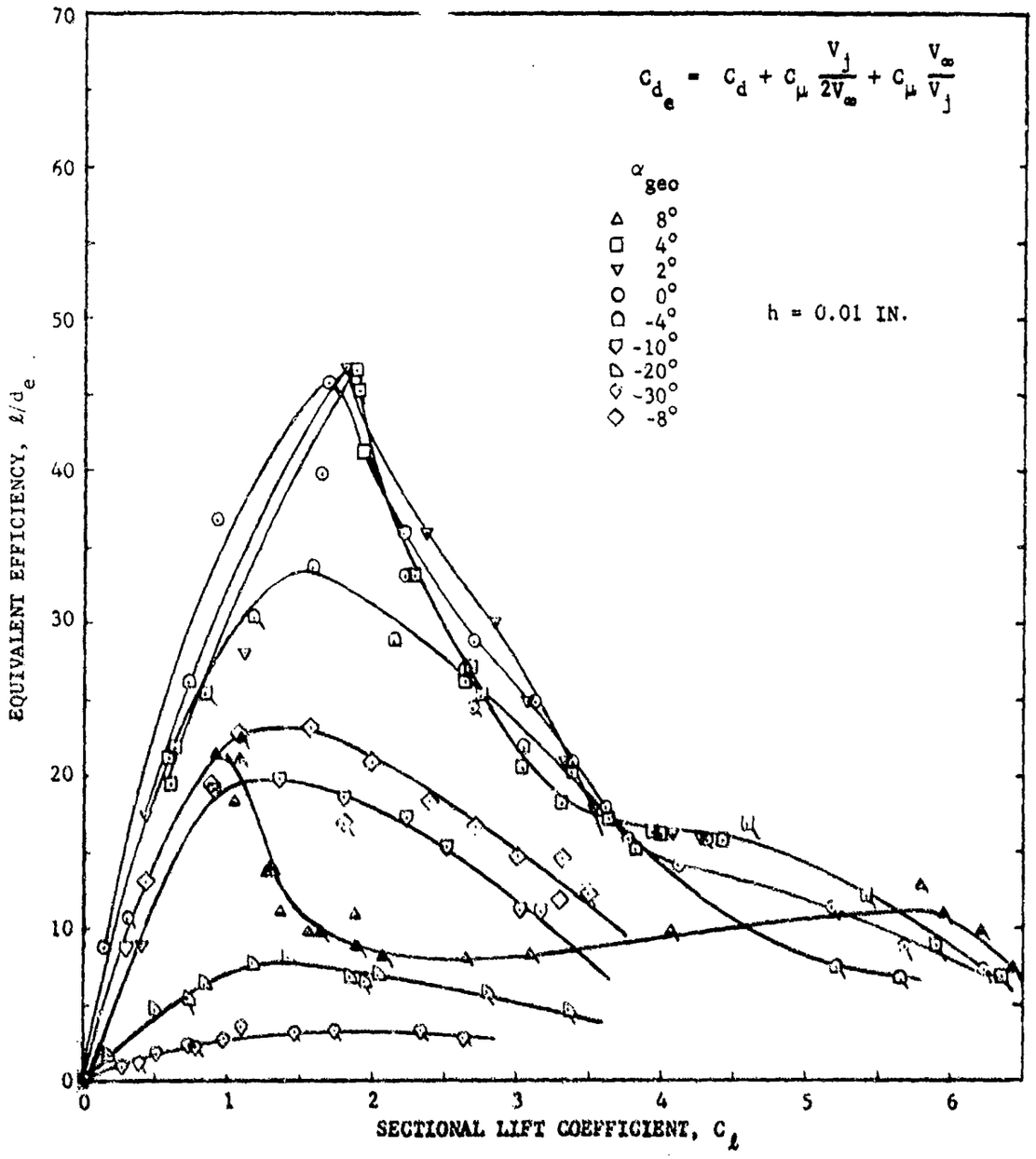

Figure 30 - Equivalent Lift-Drag Ratio as a Function of Lift Coefficient

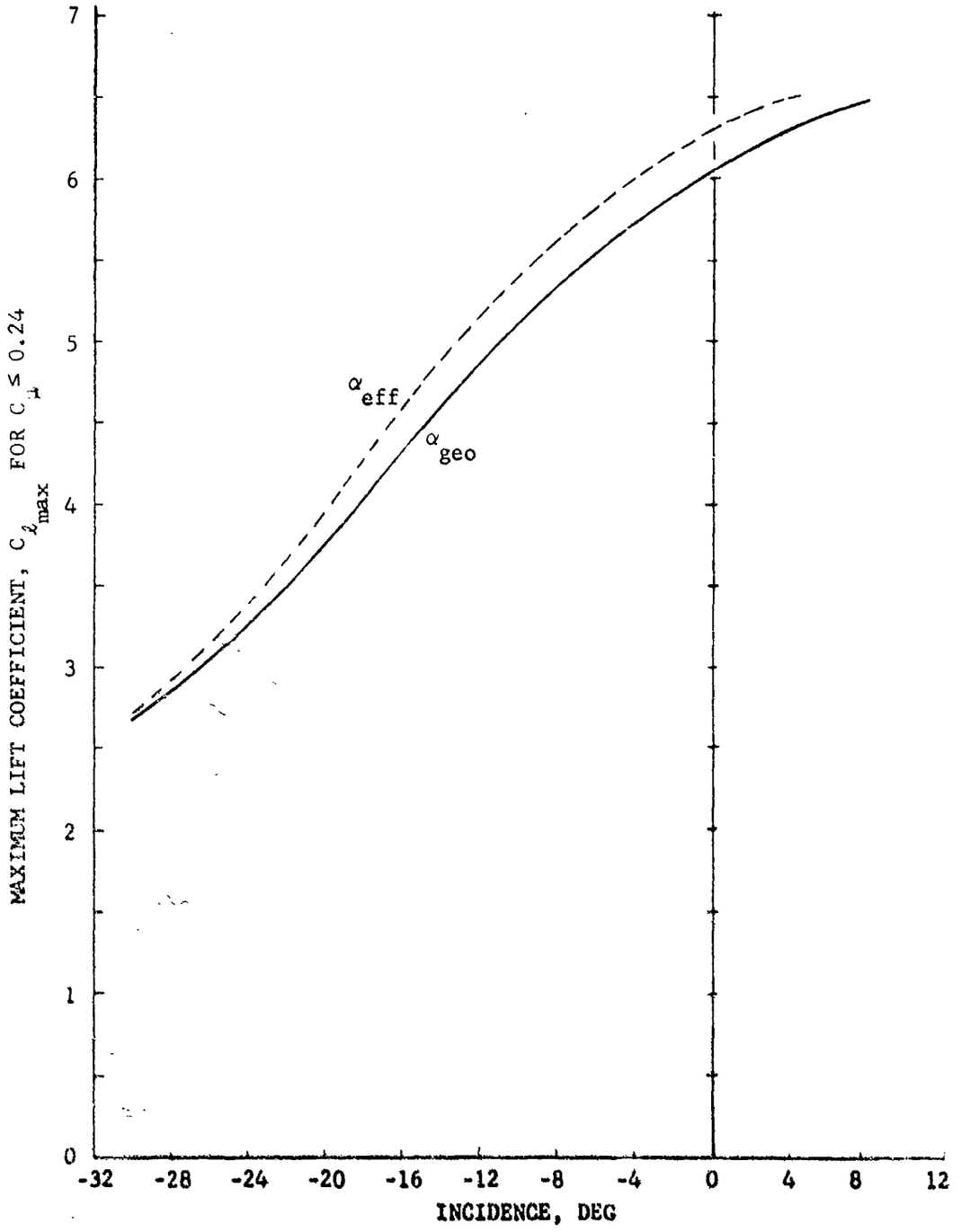

Figure 31 - Maximum Lift Coefficient as a Function of Geometric and Effective Incidence ($C_\mu \leq 0.24$, h = 0.01 Inch)

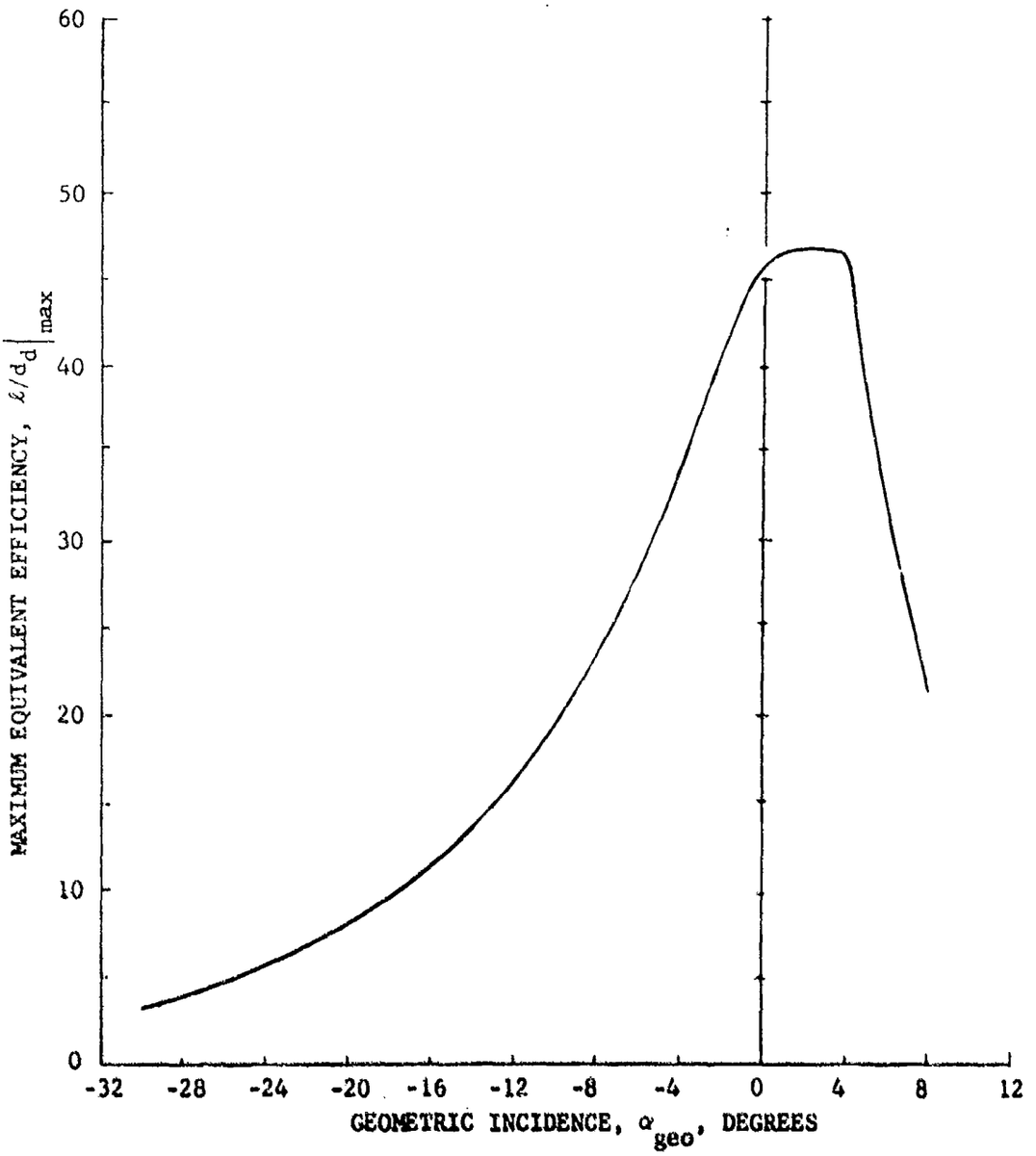

Figure 32 - Maximum Equivalent Efficiency as a Function of Geometric Incidence (h = 0.01 Inch)

UNCLASSIFIED

Security Classification

DOCUMENT CONTROL DATA - R & D

(Security classification of title, body of abstract and indexing annotation must be entered when the overall report is classified)

1 ORIGINATING ACTIVITY (Corporate author)
Aviation and Surface Effects Department
Naval Ship Research and Development Center
Bethesda, Maryland 20034

2a. REPORT SECURITY CLASSIFICATION
UNCLASSIFIED

2b. GROUP

3 REPORT TITLE

TWO-DIMENSIONAL SUBSONIC WIND TUNNEL INVESTIGATIONS OF A CAMBERED 30-PERCENT THICK CIRCULATION CONTROL AIRFOIL

4 DESCRIPTIVE NOTES (Type of report and inclusive dates)
Technical Note

5 AUTHOR(S) (First name, middle initial, last name)

Robert J. Englar

6 REPORT DATE	7a. TOTAL NO. OF PAGES	7b. NO. OF REFS
May 1972	60	15

8a. CONTRACT OR GRANT NO	9a. ORIGINATOR'S REPORT NUMBER(S)
b PROJECT NO	Technical Note AL-201
c WF 421.210	9b. OTHER REPORT NO(S) (Any other numbers that may be assigned this report)
d NSRDC 690-100	

10 DISTRIBUTION STATEMENT
Distribution limited to U.S. Government agencies only; Test and Evaluation, May 1972. Other requests for this document must be referred to Head, Aviation and Surface Effects Department (16).

11 SUPPLEMENTARY NOTES	12 SPONSORING MILITARY ACTIVITY
	Naval Material Command (03L4) Washington, D.C. 20360

13 ABSTRACT

A relatively thick Circulation Control (CC) elliptic airfoil section with thickness-to-chord ratio of 0.30 and a circular arc camber of 1.5 percent at the midchord was tested subsonically to determine its aerodynamic properties as a midspan blade section on a blown helicopter rotor. The two-dimensional tests established the section's ability to generate the required lift at low and negative incidence. Lift coefficients up to 6.5 were produced at moderate momentum coefficient ($C_\mu \leq 0.24$). High drag of the unblown bluff ellipse was greatly reduced by the application of very moderate blowing, and equivalent efficiencies of 47 (including power required for blowing) were generated at $C_\ell \approx 1.9$. The section's performance was found to be heavily influenced by upper and lower aft surface flow separations, especially at the larger positive and negative angles of attack. In addition, both low Reynolds number and an increase in slot height were detrimental to section lift capability. Nevertheless, the ability to operate at high lift coefficients essentially independent of angle of attack, and with large lift augmentation for relatively low blowing, promises to provide an effective blade section for heavy lift application.

DD FORM 1 NOV 68 1473 (PAGE 1)

S/N 0101-807-6801

UNCLASSIFIED

Security Classification

14 KEY WORDS	LINK A		LINK B		LINK C	
	ROLE	WT	ROLE	WT	ROLE	WT
high lift						
circulation control						
elliptic airfoils						
tangential blowing						
two-dimensional airfoil						
subsonic wind tunnel						
helicopter blade airfoil						
bluff airfoil						

ERRATA for

NSRDC Technical Note AL-201

page 15 - line immediately preceding equation (8), should read "... nondimensionalized by qc" - (qS is used only in experimental determination of C_μ)

page 23, Figure 2 - curve identification, both figures, should be

———— r/c = .100

-------- .075

— — — .060

— - — - .045

page 28, Figure 7 - symbol identification would be: ⊡ $\alpha_{geo} = +4°$

⊙ $\alpha_{geo} = 0°$

page 53, Figure 32 - vertical axis label should be $\ell/d_e\big|_{max}$

page 31, Figure 10 - The label $C_\mu = 0.10$ does not refer to the $\ell/de\big|_{max}$ curve, but rather to a curve which was omitted (and should run through the 0.10 label and parallel to the $C_\mu = .075$ curve). The $\ell/de\big|_{max}$ curve does not correspond to a constant value of C_μ.